



The Southern Ocean deep mixing band emerges from a competition between winter buoyancy loss and upper stratification strength

Romain Caneill¹, Fabien Roquet¹, and Jonas Nycander²

¹Department of Marine Sciences, University of Gothenburg, Gothenburg, Sweden

²Department of Meteorology, Stockholm University, Stockholm, Sweden

Correspondence: Romain Caneill (romain.caneill@gu.se)

Received: 18 October 2023 – Discussion started: 19 October 2023

Revised: 16 February 2024 – Accepted: 21 February 2024 – Published: 19 April 2024

Abstract. The Southern Ocean hosts a winter deep mixing band (DMB) near the Antarctic Circumpolar Current's (ACC) northern boundary, playing a pivotal role in Subantarctic Mode Water formation. Here, we investigate what controls the presence and geographical extent of the DMB. Using observational data, we construct seasonal climatologies of surface buoyancy fluxes, Ekman buoyancy transport, and upper stratification. The strength of the upper-ocean stratification is determined using the columnar buoyancy index, defined as the buoyancy input necessary to produce a 250 m deep mixed layer. It is found that the DMB lies precisely where the autumn–winter buoyancy loss exceeds the columnar buoyancy found in late summer. The buoyancy loss decreases towards the south, while in the north the stratification is too strong to produce deep mixed layers. Although this threshold is also crossed in the Agulhas Current and East Australian Current regions, advection of buoyancy is able to stabilise the stratification. The Ekman buoyancy transport has a secondary impact on the DMB extent due to the compensating effects of temperature and salinity transports on buoyancy. Changes in surface temperature drive spatial variations in the thermal expansion coefficient (TEC). These TEC variations are necessary to explain the limited meridional extent of the DMB. We demonstrate this by comparing buoyancy budgets derived using varying TEC values with those derived using a constant TEC value. Reduced TEC in colder waters leads to decreased winter buoyancy loss south of the DMB, yet substantial heat loss persists. Lower TEC values also weaken the effect of temperature stratification, partially compensating for the effect of buoyancy loss damping. TEC modulation impacts both the DMB characteristics and its meridional extent.

1 Introduction

The Southern Ocean (SO) plays a crucial role in global climate dynamics (Rintoul, 2018). The Antarctic Circumpolar Current (ACC), a defining feature, is demarcated by key fronts (Fig. 1): the Northern Boundary (NB), the Subantarctic Front (SAF), the Polar Front (PF), the Southern Antarctic Circumpolar Current Front (SACCF), and the Southern Boundary (SB) (Orsi et al., 1995; Park et al., 2019). These fronts mark distinct regions of water masses with varying properties and stratification (Pauthenet et al., 2017). Temperature is the stratifying agent north of the SAF in the Atlantic and Indian sectors of the SO (Pollard et al., 2002), a regime known as the alpha ocean (Carmack, 2007). Between the SAF and the PF, both temperature and salinity increase stratification in the so-called polar transition zone (Caneill et al., 2022). Finally, salinity is the only stratifying agent in the beta ocean south of the PF.

A striking phenomenon known as the deep mixing band (DMB) emerges during winter in the SO (DuVivier et al., 2018). Situated mostly north of the SAF (Fig. 1 and Dong et al., 2008), this narrow band of intense vertical mixing is of paramount importance in shaping the ocean's thermal and dynamic structure. The DMB is characterised by mixed layers (MLs) deeper than 250 m in winter. Intense buoyancy loss due to winter heat release deepens the ML, and the Ekman transport of cold water intensifies it (Naveira Garabato et al., 2009; Holte et al., 2012; Rintoul and England, 2002). This distinctive feature is found in both the Indian and Pacific sectors of the SO and underpins the formation of the Subantarctic Mode Water (SAMW) (Belkin and Gordon, 1996; Speer et al., 2000; Hanawa and Talley, 2001; Sallée et al.,

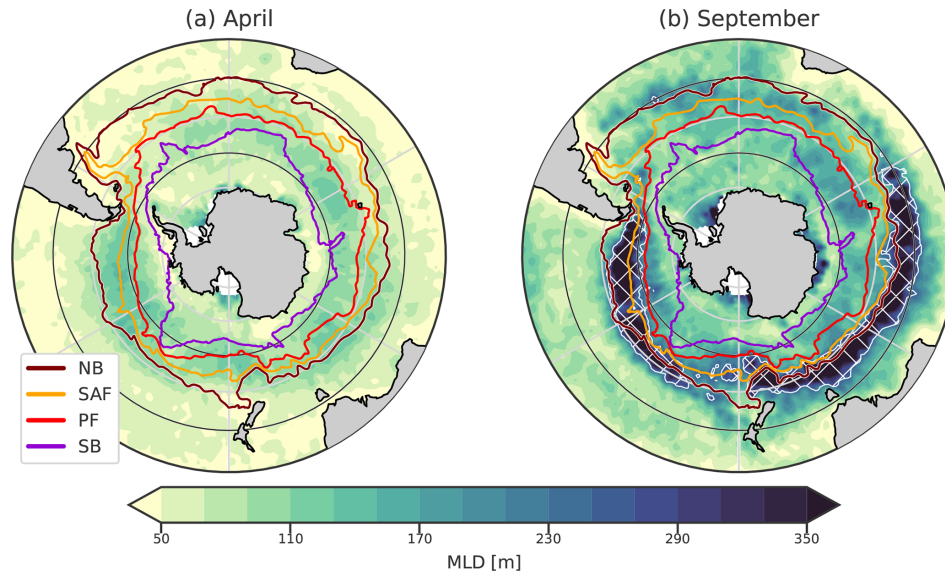


Figure 1. Mixed-layer depth (MLD) climatology in the SO with the major ACC fronts in (a) April and (b) September. From north to south, the NB (maroon colour), SAF (yellow), PF (red), and SB (purple) fronts from Park et al. (2019) are plotted. The MLDs are from de Boyer Montégut (2023). Hatching and the white contour represent the DMB. For these maps, and for the following maps of this paper, the northern boundary is at 30° S. In latitude, grid lines are spaced every 10°, with black lines at 40 and 60° S.

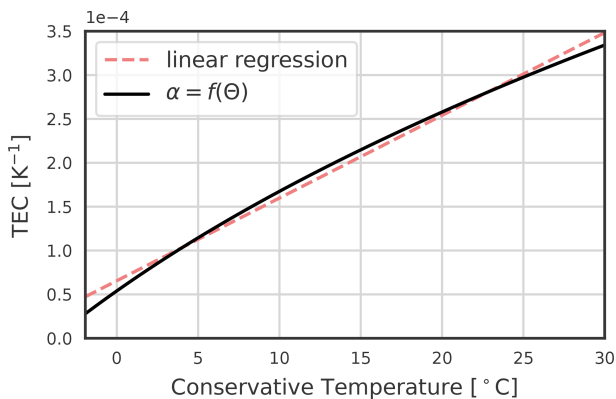


Figure 2. Thermal expansion coefficient function of Conservative Temperature. The pressure is 0 dbar, and the Absolute Salinity is 35.5 g kg⁻¹. The graph stops at -1.9 °C, the freezing point.

2010; Cerovečki et al., 2013; Cerovečki and Mazloff, 2016; Klocker et al., 2023). The SAMW, a conduit for heat and carbon exchange, exerts significant influence on the global oceanic circulation and climate processes as it forms a major component of the upper limb of the global overturning circulation (Sloyan and Rintoul, 2001). By its capacity to take up anthropogenic CO₂, it is a key component of the Earth's climate (Sabine et al., 2004).

The DMB is a major site for the uptake of anthropogenic heat and carbon from the surface to the interior (Roemmich et al., 2015; Frölicher et al., 2015; Gruber et al., 2019; Li et al., 2023); however, the physics controlling both its location and latitudinal extent remains insufficiently understood

(DuVivier et al., 2018; Fernández Castro et al., 2022). Holte et al. (2012) argued that the strength of the summer stratification determines the potential of the water column to form a deep ML in the following winter. The stratification in summer is decreased by enhanced vertical mixing (Sloyan et al., 2010), eddy-driven jet-scale overturning circulation (Li and Lee, 2017), and wind-stress-curl-induced upwelling (Dong et al., 2008). Downstream of the Agulhas Retroflection and downstream of the Campbell Plateau, eddy diffusion of heat has a tendency to stabilise the mixed layer (Sallée et al., 2006, 2008), and the spring and summer heat gain contributes to increase stratification. The geostrophic flow is roughly oriented along the isotherms and does not induce any large horizontal heat fluxes in the SO, away from western boundary currents (Dong et al., 2007). In contrast, a subsurface salinity maximum advected from subtropical water is present in most of the SO in summer, decreasing stratification below it (DuVivier et al., 2018). This salinity-driven weakening of stratification could be compensated for by temperature stratification.

Another effect relates to the nonlinear nature of the equation of state for seawater, known to play a role in the formation of Antarctic Intermediate Water (Nycander et al., 2015). The density change induced by temperature is scaled by the thermal expansion coefficient (TEC, α), defined as follows:

$$\alpha = - \left. \frac{1}{\rho} \frac{\partial \rho}{\partial \Theta} \right|_{S_A, p}, \quad (1)$$

using Conservative Temperature Θ and Absolute Salinity S_A (IOC et al., 2015). The TEC also scales the contribution of

heat fluxes to buoyancy fluxes. The TEC is a function of temperature and pressure and follows a quasi-linear relationship with temperature at the surface (Fig. 2). It is about 10 times smaller at -1.8°C than at 30°C . This effect makes the density of cold water less sensitive to temperature changes than that of warm water, enhancing the role of salinity and minimising the influence of heat fluxes on buoyancy fluxes in polar regions (Bryan, 1986; Aagaard and Carmack, 1989; Roquet et al., 2015). Variations in the TEC value also imply that winter heat fluxes have less impact on density than summer heat fluxes. Schanze and Schmitt (2013) showed that variations in the TEC increase the global buoyancy flux by 35 % due to seasonal effects. The variations in the value of the TEC allow for a total non-zero buoyancy flux while having a zero net heat flux (Garrett et al., 1993; Zahariev and Garrett, 1997; Hieronymus and Nycander, 2013). The global stratification distribution is very sensitive to changes in the TEC value (Roquet et al., 2015; Nycander et al., 2015). Its low value in the polar regions is the fundamental mechanism that allows the maintenance of a halocline under large cooling conditions and thus strongly promotes sea ice formation (Roquet et al., 2022).

Using numerical simulations of an idealised closed basin, Caneill et al. (2022) studied the impact of buoyancy fluxes in setting the position of the deep MLs, the equivalent of a DMB in their simulations. In their closed-basin study, they determined that the inversion of the sign of annual buoyancy fluxes primarily drives the poleward extent of the deep mixed layers. These buoyancy fluxes resulted from a competition between heat loss and freshwater gain. The inversion was, however, not driven by either an increase in freshwater fluxes or a decrease in heat loss. Rather, it was driven by the decrease in the TEC value in cold water, which strongly reduced the heat flux contribution to buoyancy fluxes towards the pole. The competition between heat and freshwater fluxes is thus unequal in polar regions. It is not clear whether a simple link between the DMB position and buoyancy fluxes still holds in the SO and if the variations of the TEC are sufficient to constrain the poleward extent of the DMB. In fact, the position of the DMB is not correlated with a unique component of the surface forcing, which includes wind stress, wind stress curl, buoyancy flux, and mesoscale eddy activity (DuVivier et al., 2018).

Here, we aim to characterise the dominant control of the position of the DMB in the SO by the interplay of buoyancy fluxes and stratification. For this, we create climatologies of buoyancy fluxes and stratification and compare their respective intensities. The effect of the Ekman transport is added as an extra term in the buoyancy fluxes. Measuring surface buoyancy fluxes presents challenges, entailing significant uncertainties within the SO (Cerovečki et al., 2011; Swart et al., 2019), so we focus on the climatological state of the ocean. Both seasonal and annual fluxes are taken into account, and the focus for stratification is late summer, after preconditioning has occurred, just before the ML starts to deepen. Addi-

tionally, we also aim to characterise the impact of the variations in the TEC value on the width of the DMB. For this, we compare the climatologies computed with modified TEC values.

This paper is organised as follows. First, we present the data used in this study. We then describe the equations that govern buoyancy fluxes, the Ekman transport, and stratification intensity. We continue by describing the results, and we end with a discussion and conclusions.

2 Data and methodology

Here, we describe how we constructed the climatologies for buoyancy fluxes and stratification (both its strength and thermohaline components). The general methodology consists of computing monthly components of the buoyancy fluxes for each year before averaging to produce monthly climatologies. The buoyancy fluxes are computed at a $1^{\circ} \times 1^{\circ}$ spatial resolution. We used the years 2005 to 2016 for all fluxes, as this is the record period of the ISCCP-FH MPF product (providing short-wave and long-wave heat fluxes). The stratification is computed using the Monthly Isopycnal & Mixed-layer Ocean Climatology (MIMOC), provided at $0.5^{\circ} \times 0.5^{\circ}$ spatial resolution (Schmidtke et al., 2013).

2.1 Buoyancy fluxes

2.1.1 Surface buoyancy fluxes

Surface buoyancy fluxes are defined from heat and freshwater fluxes (e.g. Gill and Adrian, 1982):

$$\mathcal{B}^{\text{surf}} = \underbrace{\frac{g\alpha}{\rho_0 C_p} Q_{\text{tot}}}_{\mathcal{B}_{\Theta}^{\text{surf}}} - \underbrace{\frac{g\beta S}{\rho_0} (E - P - R)}_{\mathcal{B}_S^{\text{surf}}} \quad (2)$$

where g is the gravity acceleration, $C_p \simeq 3997 \text{ J kg}^{-1} \text{ K}^{-1}$ the heat capacity, Q_{tot} the total heat flux in W m^{-2} , E the evaporation, P the precipitation, R the river runoff both in $\text{kg m}^{-2} \text{ s}^{-1}$, and S the surface salinity. $\mathcal{B}_{\Theta}^{\text{surf}}$ is the heat contribution, $\mathcal{B}_S^{\text{surf}}$ the salt contribution, and $\mathcal{B}^{\text{surf}}$ the total surface buoyancy flux in $\text{m}^2 \text{ s}^{-3}$.

Q_{tot} is divided into four components: net long-wave radiation (Q_{LW}), net short-wave radiation (Q_{SW}), latent heat (Q_{LH}), and sensible heat (Q_{SH}). Monthly latent and sensible heat fluxes are taken from the monthly means Objectively Analyzed Air–Sea Fluxes 1 degree dataset (OAflux; Yu and Weller, 2007) (these fluxes are only provided for oceans free of ice) and ISCCP-FH MPF (monthly means) for the short and long waves (Schiffer and Rossow, 1983; Rossow and Schiffer, 1999). The TEC is computed using the sea surface temperature (SST) provided by OAflux, and the surface salinity is taken from Estimating the Circulation and Climate of the Ocean (ECCO) Version 4, Release 4 (Forget et al.,

2015). ECCO monthly outputs have been bilinearly interpolated from the tiles onto a 1° longitude–latitude grid using the SciPy Python library (Virtanen et al., 2020).

Due to the difficulties in computing the turbulent fluxes, the total heat budget is not closed. Following Schanze and Schmitt (2013), we remove the global average (time, longitude, and latitude) of the heat and freshwater fluxes to balance them. Before adjustment, the average of the heat fluxes is 24.49 W m^{-2} , and the average integrated freshwater imbalance is -0.2 Sv . Compared to the heat and buoyancy fluxes derived from ECCO, it is found that the patterns of heat and buoyancy gain or loss are better represented after correction (Appendix A).

Freshwater fluxes combine OAflux for evaporation, Global Precipitation Climatology Project (GPCP) Version 2.3 for precipitation (Adler et al., 2018), and ECCO for river runoff.

Two seasonal components are necessary to complement the annual mean of the fluxes: buoyancy loss and buoyancy gain. We split the annual buoyancy flux into its negative and positive components: the “cooling season” (CS) and the “warming season” (WS). The cooling season is defined by the months April to September (included) and the warming season by the months October to March (included). This division captures an overview of buoyancy loss and gain throughout the seasons.

Sea ice formation and melting are associated with freshwater fluxes at the surface of the ocean. In the Southern Ocean, sea ice mostly forms close to the Antarctic coast and melts more uniformly after being exported away by wind and oceanic currents (Holland and Kwok, 2012). In the sea-ice-covered area, winter heat fluxes are small, and brine rejection when sea ice is forming is the main component of buoyancy fluxes (Klocker et al., 2023). In summer, buoyancy fluxes are positive as sea ice melts and the ocean warms up (Pellichero et al., 2018). In this study, we focus on the DMB located north of and within the ACC, which is free of ice all year. Therefore, we will not take sea ice formation or melting into account in our buoyancy flux calculations.

2.1.2 Ekman buoyancy fluxes

The Ekman transport advects heat and salt, which leads to lateral buoyancy fluxes. As is commonly done, we assume that the Ekman depth is contained within the ML (e.g. Qiu and Kelly, 1993; Sallée et al., 2006; Dong et al., 2007), so Ekman transport acts to modulate the buoyancy forcing seen at the bottom of the ML.

Associating the Ekman depth with the mixed-layer depth (MLD) comes from the fact that the turbulent viscosity should be large in the ML and small below. However, this is not obvious; studies do not always agree, depending on the region and method. Lenn and Chereskin (2009) found that viscosity decreased from approximately $0.1 \text{ m}^2 \text{ s}^{-1}$ at 26 m depth to near zero at 90 m in the Drake Passage using acoustic Doppler current profiler (ADCP) measurements of veloc-

ity. In contrast, Roach et al. (2015) found that a model with a vertically uniform viscosity between 0.05 and $0.25 \text{ m}^2 \text{ s}^{-1}$ represented the observed spirals well. Nevertheless, despite the lack of observations of the Ekman depth in the SO, Dong et al. (2007) found that using the MLD as the Ekman depth was giving accurate results in the mixed-layer heat budget. Furthermore, the ageostrophic velocities within the Ekman layer decrease with depth, so most of the transport occurs closer to the surface than to the bottom of the Ekman layer. Thus, if the Ekman depth is slightly larger than the MLD, the transport within the ML will only be slightly overestimated.

To compute buoyancy fluxes, one needs to compute the Ekman horizontal transport ($U_{\text{Ek}}, V_{\text{Ek}}$) (e.g. Qiu and Kelly, 1993; Yang, 2006):

$$-fV_{\text{Ek}} = \frac{\tau^x}{\rho} \quad \text{and} \quad fU_{\text{Ek}} = \frac{\tau^y}{\rho}, \quad (3)$$

where (τ^x, τ^y) are the (x, y) components of the wind stress. Using the heat and freshwater fluxes due to horizontal Ekman advection,

$$Q_{\text{Ek}} = \rho_0 C_p U_{\text{Ek}} \cdot \nabla \Theta, \quad (4)$$

$$\text{FW}_{\text{Ek}} = \frac{\rho_0}{S} U_{\text{Ek}} \cdot \nabla S, \quad (5)$$

where Θ is the Conservative Temperature and S the Absolute Salinity. The Ekman transport is derived from wind stress using Eq. (3), leading to

$$\mathcal{B}_{\Theta}^{\text{Ek}} = -\frac{g\alpha}{\rho_0 f} \left(\tau^y \frac{\partial \Theta}{\partial x} - \tau^x \frac{\partial \Theta}{\partial y} \right), \quad (6)$$

$$\mathcal{B}_S^{\text{Ek}} = \frac{g\beta}{\rho_0 f} \left(\tau^y \frac{\partial S}{\partial x} - \tau^x \frac{\partial S}{\partial y} \right). \quad (7)$$

\mathcal{B}^{Ek} are fluxes within the Ekman layer. Under the assumption that the Ekman layer is contained within the ML, \mathcal{B} , the sum of \mathcal{B}^{Ek} and $\mathcal{B}^{\text{surf}}$, corresponds to the buoyancy flux taken at the base of the ML. \mathcal{B}^{CS} is the total buoyancy loss during the cooling season, defined by taking the mean of \mathcal{B} during the cooling season.

We computed daily averages of wind stress from the CMEMS “Global Ocean Wind L4 Reprocessed 6 Hourly Observations”. To compute horizontal gradients of temperature and salinity, we used the ARMOR3D weekly product (Guinehut et al., 2012). We took the average of the three upper levels (0, 5, and 10 m) and then did a linear interpolation in time to get daily data.

2.2 Stratification from columnar buoyancy

We quantify the stratification using the columnar buoyancy (Lascaratos and Nittis, 1998; Herrmann et al., 2008; Lee et al., 2011; Small et al., 2021):

$$CB(Z) = \int_Z^0 -zN^2(z)dz, \tag{8}$$

where z is depth, and the z -axis oriented upward. Z is the depth at which the columnar buoyancy is computed. $N^2(z)$ is calculated using the locally referenced potential density. For shallow depths, an approximation using the potential density referenced at the surface is applicable. By integrating Eq. (8) with this approximation, a formula directly using potential density profiles is obtained:

$$CB(Z) \simeq \frac{g}{\rho_0} \int_Z^0 [\rho_\theta(Z) - \rho_\theta(z)]dz. \tag{9}$$

The columnar buoyancy, positive under stable stratification, quantifies the vertically integrated amount of buoyancy that must be lost to create a ML of depth Z . We compute this index in April, which corresponds to the most stratified water column before it is eroded during the cooling season. Dividing $-CB$ by a time Δt gives the buoyancy fluxes necessary to deepen the ML to Z during Δt (Faure and Kawai, 2015):

$$B_{250} = \frac{-CB(-250)}{\Delta t}. \tag{10}$$

We compute the columnar buoyancy at a depth of 250 m, the threshold in mixed-layer depth used to define the DMB (Duvivier et al., 2018). We compute B_{250} in April, just before the cooling season, so $(B_{250} - \mathcal{B}^{CS})$ estimates the columnar buoyancy at the end of winter. Thus, the comparison of B_{250} with the buoyancy loss directly informs if the buoyancy fluxes can produce a mixed layer of 250 m. We emphasise that using another value of the threshold does not change any conclusions of this paper (Fig. C1 in Appendix C). We used $\Delta t = 6$ months to allow comparison with the mean buoyancy loss of the cooling season (Sect. 2.1.1). B_{250} is negative for stable stratification.

The influence of temperature and salinity alone on stratification is done by separating their effects, as has been similarly done by Sterl and De Jong (2022). B_{250} can thus be split using the decomposition of the buoyancy frequency into the thermal and haline components:

$$B_{250} = \underbrace{\frac{g}{\Delta t} \int_{-250}^0 \alpha(z) \frac{\partial \Theta}{\partial z} z dz}_{B_{250}^\Theta} - \underbrace{\frac{g}{\Delta t} \int_{-250}^0 \beta(z) \frac{\partial S}{\partial z} z dz}_{B_{250}^S}, \tag{11}$$

We expect B_{250}^Θ to be negative north of the PF (stabilising effect of temperature) and positive south of it (destabilising effect), while B_{250}^S should be positive north of the SAF and negative south of it.

The columnar buoyancy is computed using Monthly Isopycnal & Mixed-layer Ocean Climatology (MIMOC) in depth coordinates (Schmidtko et al., 2013).

2.3 Effect of the variations of the TEC

The TEC scales the effect of heat fluxes on buoyancy fluxes and determines the importance of temperature for stratification. To investigate how the TEC variations affect stratification and buoyancy fluxes, we computed them using α_0 , a constant TEC characteristic of the waters in the DMB. This replacement is made in Eqs. (2), (6), and (11). It will be explicitly mentioned when the constant TEC is used and the results are presented in Sect. 4.

To compute the value of α_0 , we used the average temperature of surface water located at 40° S ($\Theta \simeq 14.7^\circ\text{C}$), a salinity of 35.5 g kg⁻¹, and a pressure of 0 dbar. The result is $\alpha_0 \simeq 2.1 \times 10^{-4} \text{K}^{-1}$. The latitude 40° S has been chosen as it roughly corresponds to the latitude located just north of the DMB.

3 Results

3.1 Annual buoyancy fluxes

Annual surface buoyancy fluxes induced by heat fluxes ($\mathcal{B}_\Theta^{\text{surf}}$) tend to be negative (cooling) north of 50° S and positive south of it, but the pattern shows large regional disparities (Fig. 3a). The DMB is associated with a net annual cooling; in the Indian and Pacific sectors, it is surrounded by regions of net annual warming. The heat loss is located north of the ACC in the Atlantic and Indian sectors, while the heat loss in the eastern Pacific sector is located within the ACC. Except for this large region of loss in the Pacific sector, even if the heat fluxes look patchy, heat is mostly gained within the ACC. This is due to large radiative heat fluxes compared to small sensible heat fluxes (Czaja and Marshall, 2015). Thus, heat fluxes are not zonally constant in the ACC (Song, 2020; Josey et al., 2023). Overall, in both the Indian and Pacific sectors of the SO, the DMB is surrounded by annual heat gain in the north and south. We note that the regions with the largest annual surface heat loss are co-located with the western boundary currents and the Leeuwin Current at the western coast of Australia due to the advection of warm water (Fig. 3a).

In contrast to the patchiness and geographical variability of $\mathcal{B}_\Theta^{\text{surf}}$, the distribution of the haline component of the surface buoyancy fluxes, $\mathcal{B}_S^{\text{surf}}$, is much smoother. Precipitation in the south and evaporation in the subtropical gyres are responsible for the global pattern of freshwater fluxes (Fig. 3b). $\mathcal{B}_S^{\text{surf}}$ is mainly positive within the DMB and positive everywhere south of it. This illustrates the fact that freshwater forcing depends little on ocean conditions, contrary to heat flux.

The sum of these two surface components, $\mathcal{B}^{\text{surf}}$, is similar to $\mathcal{B}_\Theta^{\text{surf}}$ north of the ACC (Fig. 3c). Within and south

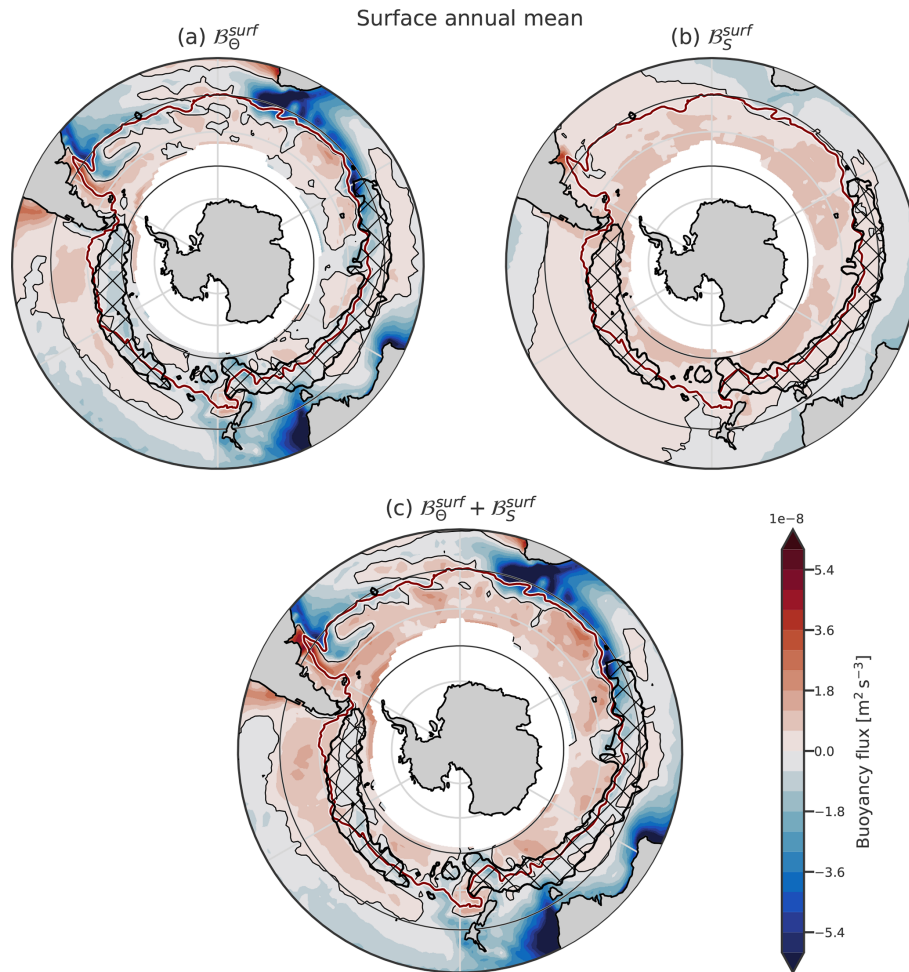


Figure 3. Climatology of the annual components of the surface buoyancy fluxes. The heat component (a), haline component (b), and their sum (c) are plotted. On every plot, the thin black lines represent the 0 point of the fluxes, while the maroon line is the northern boundary of the ACC, defined as the northernmost closed contour of mean dynamic topography, as defined by Park et al. (2019). Hatching represents the DMB. The northern boundary is at 30° S. In latitude, grid lines are spaced every 10°, with black lines at 40 and 60° S.

of the ACC, it is positive everywhere except in the Pacific sector, where the DMB occurs: a narrow band of buoyancy loss is present with a large tongue of buoyancy gain north of it. Overall, a circumpolar band of buoyancy loss is present in the SO, surrounded by buoyancy gain, particularly in the Indian and Pacific sectors. Caneill et al. (2022) found that the poleward boundary of the deep MLs region was located at the inversion of the annual buoyancy fluxes in a coarse-resolution idealised closed-basin study. The circulation in the SO differs from the one in a closed basin as considered in Caneill et al. (2022); the path of the ACC is more or less zonal, while the closed-basin circulation has an important meridional upper-ocean transport. Moreover, the ACC interacts with the bathymetry and presents large-eddy activity, two phenomena not really represented in the idealised basin of Caneill et al. (2022). Despite these differences, their conclusion that deep MLs (the DMB in the SO) are bounded poleward by the inversion of the annual buoyancy fluxes still

holds in the SO. Additionally, the DMB is also bounded equatorward by tongues of annual buoyancy gain, meaning that the DMB coincides with a narrow band of annual buoyancy loss surrounded by buoyancy gain.

3.2 Effect of the Ekman transport

The Ekman transport brings cold water northward south of about 30° S and thus creates a negative buoyancy flux at the base of the Ekman layer (Fig. 4a). The largest negative values are found around the NB of the ACC in the Indian Ocean. The SAF has a large SST meridional gradient (Kostianoy et al., 2004), which enhances the meridional advection of cold water and thus creates a large negative buoyancy flux. The Ekman salt component presents large positive values close to the NB (Fig. 4b). The temperature and salinity components of the Ekman transport strongly compensate in the vicinity of the SAF, where the SST gradients are compen-

sated by the sea surface salinity gradients (Fig. 4c). Summed together, the buoyancy fluxes induced by the Ekman transport are negative in the SO and positive in the southern part of the subtropical gyres (Fig. 4c). The negative temperature anomaly in the ocean induced by the Ekman transport creates a positive anomaly in surface heat fluxes. As a result, Ekman and atmospheric heat fluxes likely partially compensate for each other. Such partial compensation can be seen when comparing Figs. 3a and 4a and d, e.g. in the south-eastern Pacific Ocean, north of the ACC. When the Ekman contribution is included, almost all the SO south of 30° S is losing buoyancy due to heat on the annual mean.

Regions within the ACC that gain heat from the atmosphere encounter compensation from Ekman transport and are thus also losing heat on the annual mean (Fig. 4d). Although $\mathcal{B}_{\ominus}^{\text{surf}}$ is overall positive south of the NB of ACC, when the Ekman heat component is included, $\mathcal{B}_{\ominus}^{\text{tot}} = \mathcal{B}_{\ominus}^{\text{surf}} + \mathcal{B}_{\ominus}^{\text{Ek}}$ becomes negative almost everywhere in the SO (Fig. 4d). The Ekman heat transport thus has a destabilising effect that counteracts the surface heat gain. The total salt component resembles its atmospheric part while being slightly modulated by Ekman transport. \mathcal{B} is negative between the ACC and 25° S, and south of the DMB it alternates between regions of positive and negative values (Figs. 4f and 5b). It is continuously negative within the northern part of the ACC in the Pacific sector.

In short, the Ekman transport generates important fluxes of both temperature and salinity, but the net effect on the buoyancy at the bottom on the ML remains limited overall, with a few regional exceptions such as around the Kerguelen Plateau. The Ekman transport can still participate in the interannual variability of the MLD (Cerovečki et al., 2019; Li and England, 2020).

3.3 Seasonal cycle of buoyancy fluxes and upper-ocean stratification

The annual mean of $\mathcal{B}_{\ominus}^{\text{surf}}$ hides a large seasonal cycle with a large winter buoyancy loss and a large summer buoyancy gain (Fig. B1 in Appendix B). In contrast, the other components have a very small seasonal cycle compared to $\mathcal{B}_{\ominus}^{\text{surf}}$ (Fig. 5c and d). To go beyond annual buoyancy fluxes, one can compare the seasonal fluxes with the position of the DMB (Fig. 5a). One striking point is that the DMB (with MLDs deeper than 250 m) is not located in regions of the largest annual or winter buoyancy loss but south of them. The largest cooling season's buoyancy loss of about $-6 \times 10^{-8} \text{ m}^2 \text{ s}^{-3}$ is located around 30° S, where the winter MLD barely exceeds 100 m. The winter buoyancy loss is 3 times lower at 50° S, a region where deep MLs are formed. Therefore, a large winter buoyancy loss itself is not sufficient to produce deep winter ML. This is because the poleward advection of stratified water from the subtropics limits the ML deepening. Therefore, stratification strength also needs to be taken into account when studying deep ML formation.

The strength of the stratification is studied using the columnar buoyancy B_{250} (computed in April, before the cooling season), i.e. the equivalent buoyancy flux necessary to erode the summer stratification and form a 250 m deep mixed layer. The subtropical and subpolar SO are thermally stratified ($B_{250}^{\ominus} < 0$), while in the polar region the temperature component of stratification is negative (Fig. 6a). The haline stratification follows an opposite pattern, with the salinity component of stratification decreasing stratification in the subtropical regions ($B_{250}^{\text{S}} > 0$) and increasing it in the polar regions (Fig. 6b). We note that the transition from salinity destabilisation to stabilisation is located northward of the temperature inversion. The exact location of these stratification changes depends on the reference depth taken (250 m here), but the global pattern is a robust feature of the stratification from subtropical to polar environments (Carmack, 2007; Roquet et al., 2022).

In the DMB, as well as everywhere except close to Antarctica, the temperature stratifies on average in the upper 250 m in summer (Fig. 6a). The role of salinity is to stabilise the DMB in the Pacific Ocean; in the Indian Ocean, the DMB is located at the boundary between the salinity-stabilising and salinity-destabilising regimes. The presence of a salinity maximum advected from Agulhas water around 150 m deep in the region north of the ACC helps to decrease the summer stratification in the Indian Ocean (Yeager and Large, 2007; Wang et al., 2014; DuVivier et al., 2018; Fernández Castro et al., 2022).

We now consider the total stratification, $B_{250} = B_{250}^{\ominus} + B_{250}^{\text{S}}$. It is the weakest in the southern part of the SO (Figs. 7a, 8, and 9a). The strongest stratifications are found in the subtropics (dark blue colours representative of the most negative value of B_{250} , Fig. 7a). At 20° S, it reaches a value more than 5 times larger than in the polar region. A band of stratification minimums exists around the DMB (light colours, Fig. 7a). (Small et al., 2021) remarked that this minimum of stratification preconditions the DMB for the formation of deep winter MLs. Part of the existence of this minimum can be attributed to the fact that B_{250} includes the effect of the seasonal cycle of the stratification. Outside the DMB, B_{250} captures more permanent stratification than within the DMB. Weak stratification is also found outside the DMB, and the stratification minimum is not very pronounced. The general trend is that the stratification decreases from the subtropics to the polar region.

Regions where \mathcal{B}^{CS} is more negative than B_{250} have a large probability of forming a ML deeper than 250 m, unless another process not taken into account makes the water column more stable. The buoyancy loss during the cooling season, driven by heat fluxes, is the most intense around 30° S (Fig. 7b), a region where the gain in summer buoyancy is also very large. Apart from the summer buoyancy gain, this is also a region where subtropical stratified water is advected. South of this region, the winter buoyancy loss becomes smaller, so it has less potential to form a deep mixed layer. The general

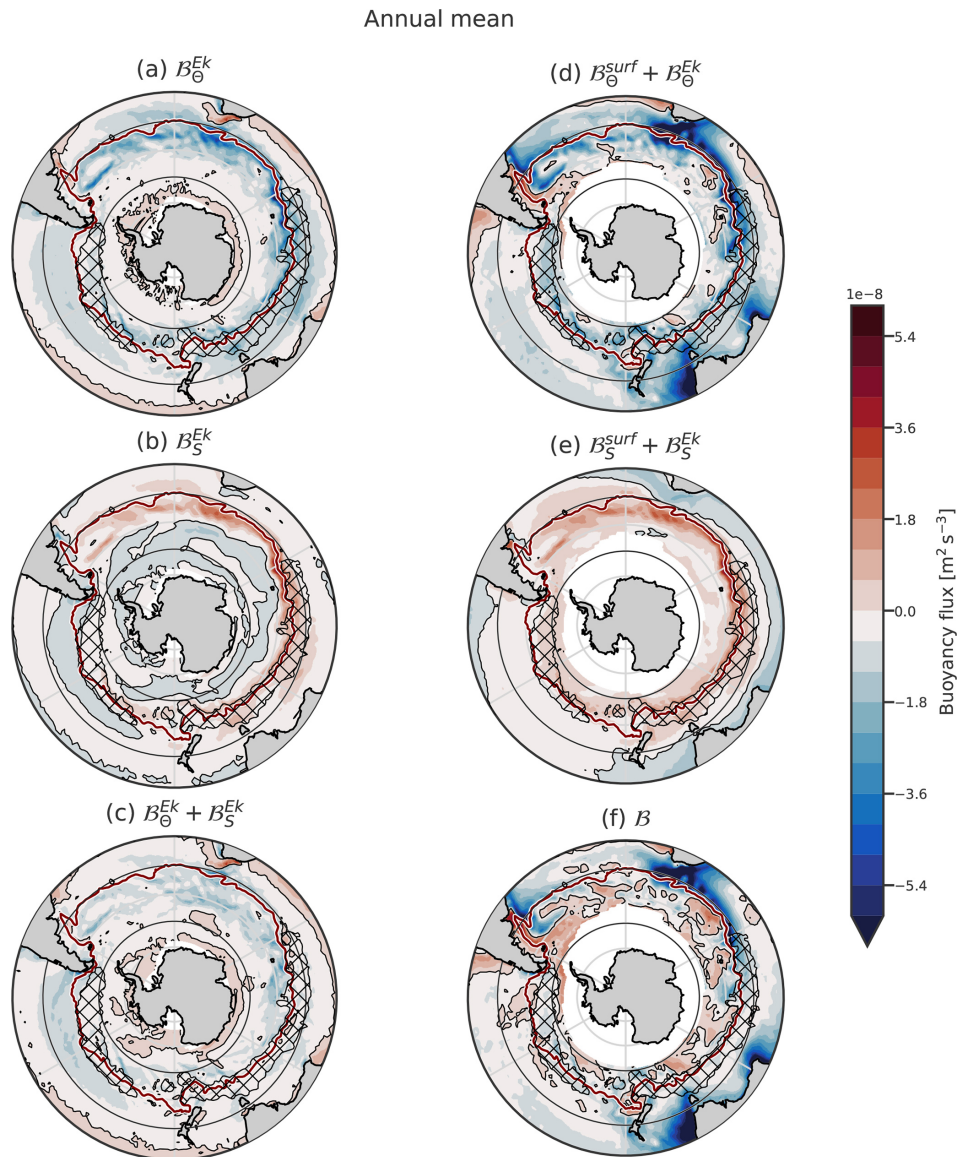


Figure 4. Climatology of the annual components of the Ekman-induced buoyancy fluxes and the sum with the surface fluxes. The subplots are organised as follows: the columns show the Ekman fluxes and the sum of Ekman and surface fluxes. The rows show the thermal component, haline component, and their sum.

pattern is that the buoyancy loss becomes smaller from 30°S poleward.

Both the buoyancy loss and the stratification decrease poleward. To assess how the balance between these two opposite effects shapes the DMB, we compare the position of the DMB with the residual $B_{250} - B^{\text{CS}}$ (Fig. 7c). MLD larger than 250 m are only found where $B_{250} > B^{\text{CS}}$ but not vice versa. The largest mismatch is located south of Africa, in the Agulhas Retroreflection region. Our analysis does not include the direct effect of advection by the geostrophic flow. However, our results strongly point to its restoring effect on the stratification in the regions of large western boundary currents such as the Agulhas Retroreflection or the East Australian current.

Overall, the simple balance between B_{250} and B^{CS} as main drivers of deep ML formation does not hold at the western boundary currents but otherwise predicts the location of the DMB with good accuracy.

The zonal sections and the zonal median show the competition between the winter buoyancy loss and the existing summer stratification (Figs. 8 and 9a). Sections in the middle of the Atlantic, Indian, and Pacific sectors of the SO are plotted. In the transect of the Atlantic sector, the MLD does not reach 250 m, but the location where buoyancy fluxes are more negative than stratification still corresponds to the position of the deepest MLD of the transect. In both the Indian and Pacific transects, there is a very good match between the

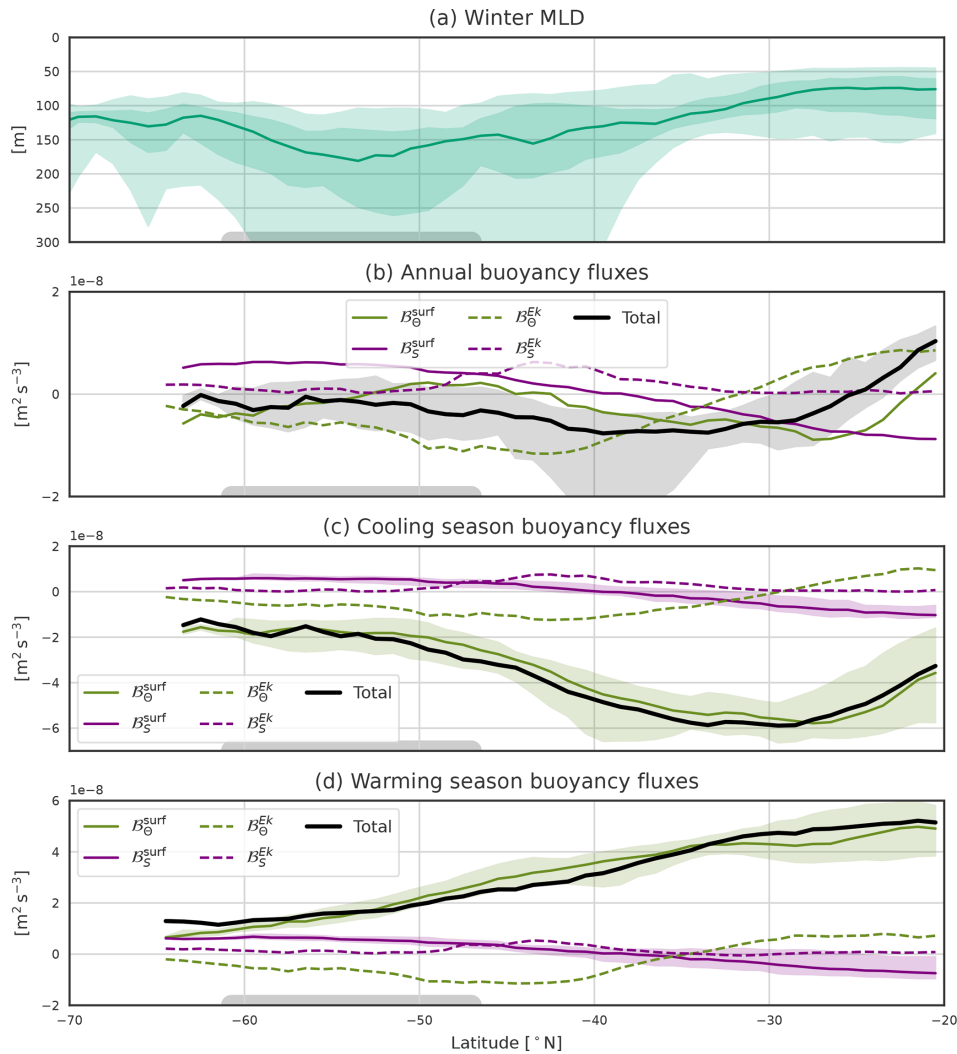


Figure 5. (a) Winter MLD. The light and dark shading represents, respectively, the 5th–95th and 25th–75th percentiles, and the solid line is the zonal median. Mixed layers deeper than 250 m are found between 40 and 60° S depending on the SO sector. (b) Annual mean of the buoyancy flux components, (c) cooling season means, and (d) warming season means. The solid lines are the zonal medians, and the shading represents the region between the 25th and 75th percentiles. The black line is B the sum of surface and Ekman fluxes. The vertical grid spacing is constant between panels. The black, green, and purple colours are for the total, heat surface, and salt surface components, respectively. The majority of the zonal differences arise from the surface heat component. The gray box at the bottom represents a median position of the ACC.

position of the DMB and the balance between the stratification and the buoyancy loss. South of the DMB, the stratification remains small, but the buoyancy loss becomes closer to zero and is not sufficient to erode this small stratification, meaning that the MLD is not deeper than 150 m. It becomes clear that only in a few locations does the winter buoyancy loss become sufficient to erode the stratification.

Despite a weak stratification south of 50° S in the Atlantic and Indian sectors, no deep ML is observed as the winter buoyancy loss is smaller there. As seen previously, the heat component of the buoyancy fluxes is scaled by the TEC, itself a function of temperature. We will now explore the importance of this mechanism.

4 Effect of the local value of the TEC

To understand how variations in the TEC value affect the SO stratification, we computed the buoyancy fluxes and the columnar buoyancy using a constant value α_0 , representative of 40° S. We use the residual of buoyancy loss and stratification to predict the geographical extent that the DMB would have in this case.

Heat fluxes are negative in winter, so south of 40° S, where α_0 is larger than the real value of the TEC, the buoyancy fluxes become more negative (blue line in Figs. 9b and 10b and c). On the contrary, the buoyancy fluxes become smaller north of 40° S. This implies that the poleward extent of the

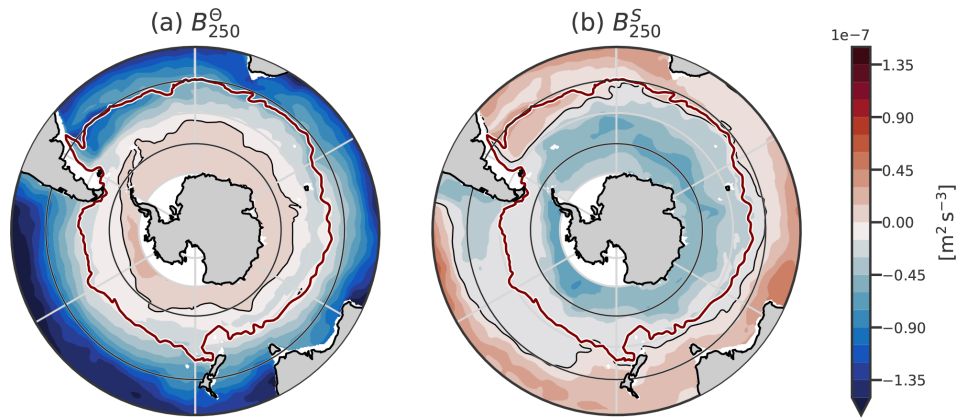


Figure 6. Climatology of (a) the thermal and (b) haline components of B_{250} , computed in April.

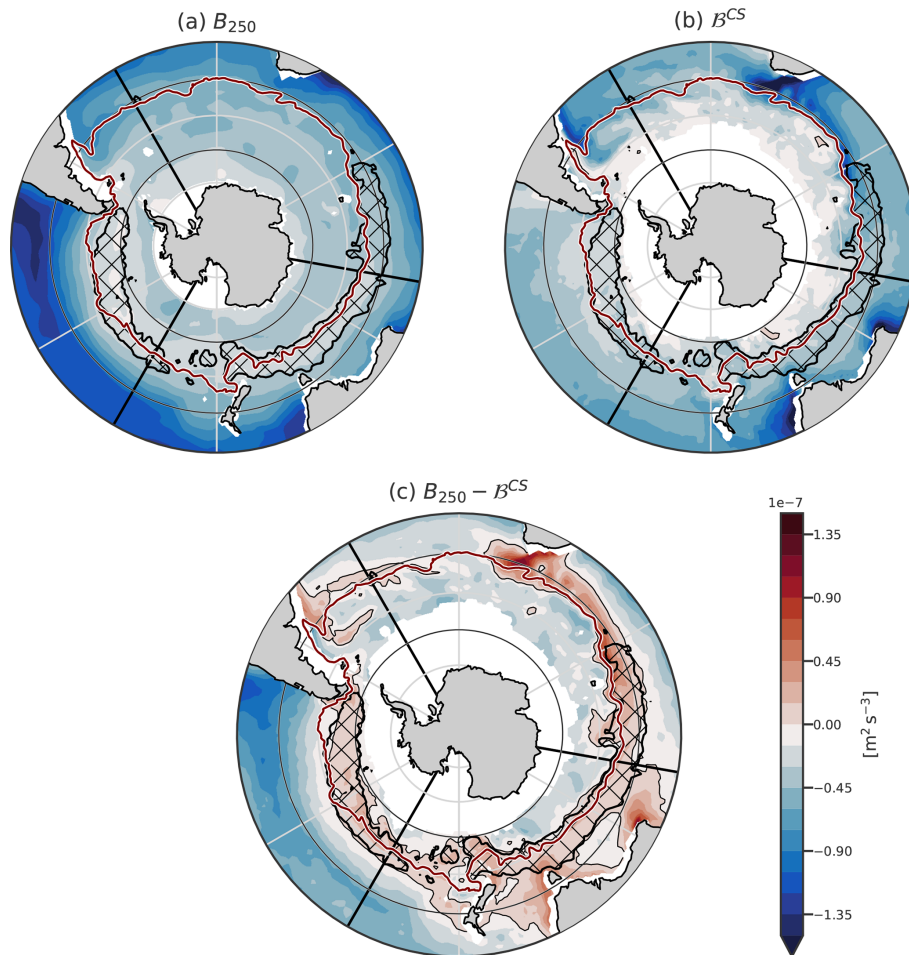


Figure 7. Climatology of (a) the intensity of late summer stratification characterised by B_{250} , (b) the buoyancy fluxes during the cooling season, and (c) the difference $B_{250} - B^{CS}$. The hatching surrounded by the black contour represents the DMB. The three black lines represent the transects plotted in Fig. 8.

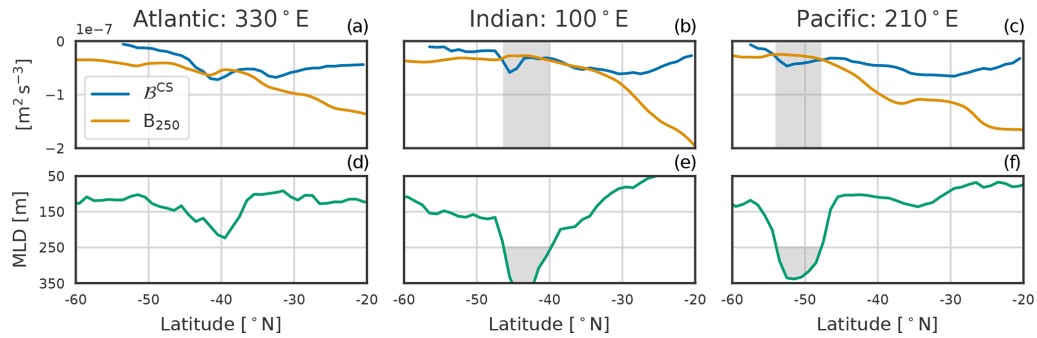


Figure 8. B_{250} (orange curves) and B^{CS} (blue curves) (a, b, c), and observed winter MLD (green curve in d, e, f), for three different transects in the Atlantic, Indian, and Pacific sectors of the SO. The gray box represents the DMB.

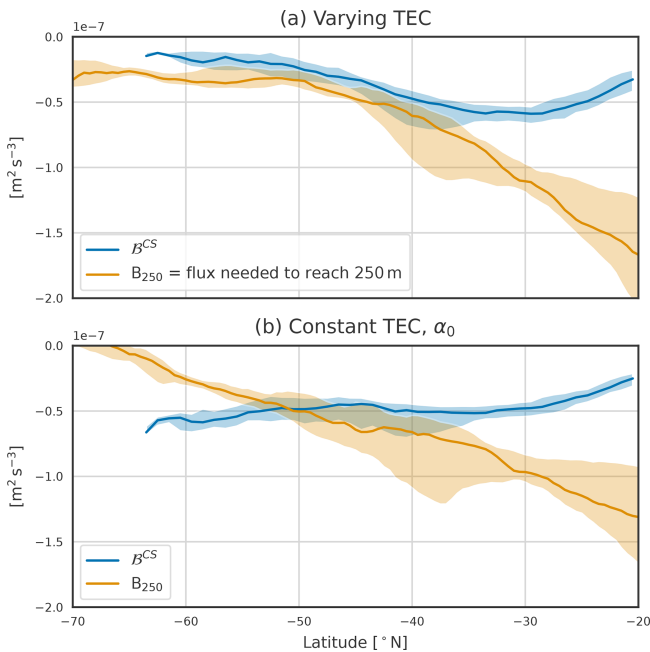


Figure 9. Buoyancy fluxes during the cooling season (blue) and B_{250} the buoyancy fluxes needed to produce a 250 m deep mixed layer (orange). Panel (a) is computed using the realistic varying TEC, and panel (b) is computed with α_0 . Shaded areas correspond to the first and third quartiles, and the solid lines are the zonal medians. The blue line corresponds to the black line of Fig. 5c. This plot extends to 20° S to highlight the increase in stratification towards the tropics and the maximum buoyancy loss located around 30° S.

DMB is primarily determined by the decrease in TEC value, which significantly dampens the impact of heat fluxes on buoyancy fluxes. It is not constrained by a decrease in winter heat loss to the south.

The TEC modulates the effect of temperature on stratification. North of 40° S, the temperature stratifies and the TEC value is larger than α_0 , so using α_0 implies a weaker stratification (orange line in Figs. 9b and 10a). ΔB_{250} , the difference between the columnar buoyancy computed with

the varying TEC and the constant TEC, is thus negative (Fig. 10b). In contrast, between 40° S and the PF, where temperature still decreases with depth and the TEC value is smaller than α_0 , stratification is strengthened. South of the temperature inversion, where colder water lies above warmer water, an increased TEC value decreases or even destabilises the stratification. Such regions are found where $\Delta B_{250} < 0$ close to Antarctica, as seen in Fig. 10. The effect of the TEC on stratification is thus not constant over all of the SO, but it is its small value that allows for the typical temperature inversion of polar regions while having a stable water column.

Where B^{CS} is more negative than B_{250} , deep MLs would be produced (Figs. 9b and 11). The global pattern of stratification strength changes slightly with the constant TEC (Fig. 11a). The stratification is weakening continuously from the subtropics towards Antarctica until it eventually becomes negative and thus unstable. The winter buoyancy loss is intense everywhere within the SO and does not decrease poleward (Fig. 11b).

In the Indian Ocean, a second region where $B_{250} - B^{CS} > 0$ appears south of the DMB (the red region close to the sea ice edge). North of this second band, around 50° S, even if B^{CS} becomes very negative due to the large value of α_0 , the stratification is also slightly stronger, which counterbalances for the larger buoyancy loss. In the Pacific Ocean, where stratification is smaller, the predicted DMB extends all the way to the sea ice edge. As the reference value for the TEC is 40° S, the northern boundary of the DMB does not change much.

The overall effect of using the constant TEC is that the southern boundary of the predicted DMB is shifted southward, up to the edge of the sea ice. The DMB formed in an ocean with a constant α_0 would overlap with the observed DMB (Fig. 11c). In the Indian Ocean, two DMBs are formed: one with the same position as the observed one, and one within the ACC close to the actual sea ice edge. In the Pacific Ocean, these two DMBs are merged into a wide one. It is likely that such deep MLs would be formed, as mean advection is more or less zonal and does not bring highly stratified waters within the ACC. The narrowness of the DMB in the Pacific basin thus arises from the decrease in the TEC,

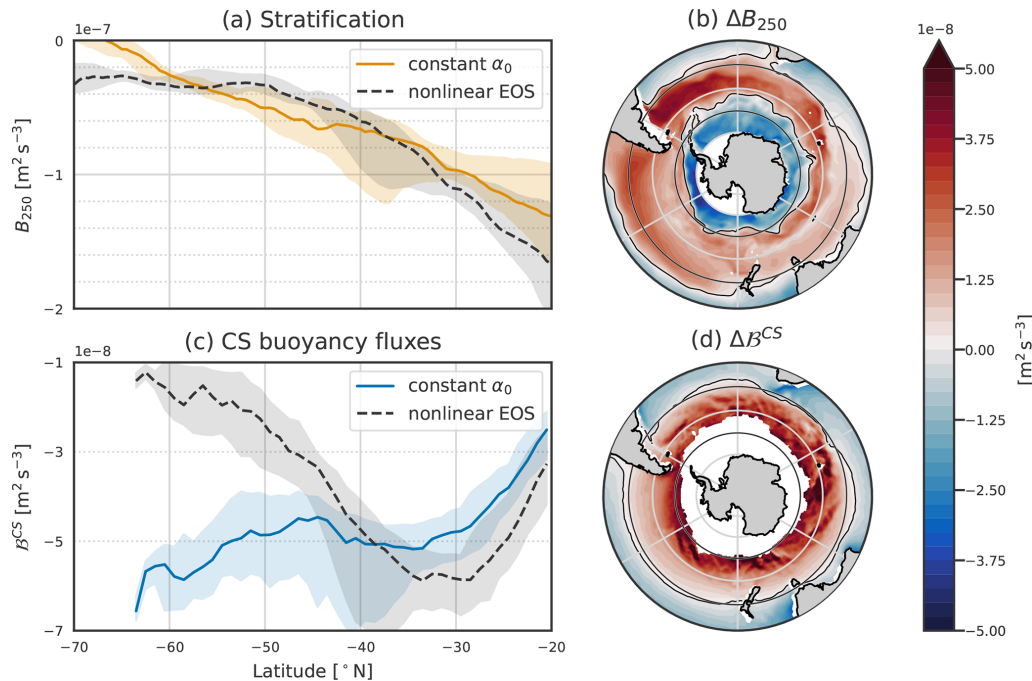


Figure 10. Stratification and buoyancy fluxes and computed using the nonlinear equation of state (EOS) or a constant α_0 . In panels (a) and (c), dashed black lines are for the nonlinear EOS, and solid blue or orange lines show constant α_0 . The spacing between the horizontal dotted gray line is the same in these two panels and equal to $2 \times 10^{-8} \text{ m}^2 \text{ s}^{-3}$. The lightly shaded areas correspond to the 25th and 75th percentiles. Panels (b) and (d) are the difference between using the varying TEC and the constant α_0 for B_{250} and B^{CS} , respectively.

which itself induces a decrease in winter buoyancy loss. In the Indian Ocean, the TEC variations prevent the formation of a second region of deep mixed layer south of the DMB.

5 Discussion and conclusions

In this study, our goal was to determine if the position of the Southern Ocean DMB and its limited latitudinal extent can be explained only by the balance between the buoyancy loss of the cooling season and the stratification intensity. We find that this balance is sufficient to predict the DMB away from large southward currents in the climatological state. The narrowness of the DMB emerges because south of it the buoyancy fluxes are small despite a weakly stratified ocean. This small buoyancy loss results from the decrease in the TEC in cold water and not from a decrease in winter heat loss towards the pole.

A perfect prediction of the DMB spatial extent is not realistic, as other processes such as wind-induced turbulence or Ekman pumping contribute to changing the ML in the SO (Holte et al., 2012; Li et al., 2022). Our study, however, highlights the first-order role of the competition between winter buoyancy loss and existing stratification in forming the DMB. North of 40° S, despite the largest buoyancy loss during the cooling season, no deep ML is produced because the stratification of the water column induced by temperature is also very strong. In contrast, within the ACC (except in

the eastern Pacific sector), the water column is only weakly stratified, but the buoyancy loss during the cooling season is small. Hence, it is only in a narrow band where winter buoyancy loss is large enough and stratification is weak enough to significantly deepen the ML.

The buoyancy fluxes follow a strong seasonal cycle, mainly driven by surface heat fluxes. South of 30° S, the Ekman transport advects cold water northward, which produces a negative heat flux. It is likely that this flux itself induces a positive heat flux from the atmosphere on an annual scale. This could explain why the negative Ekman heat flux can counterbalance the surface heat gain (Tamsitt et al., 2016). Ekman transport must therefore be taken into account when computing buoyancy fluxes in the mixed layer. Because of the variability of the wind stress, it drives a large part of the inter-annual variability of the SAMW temperature and salinity (Rintoul and England, 2002).

Even if the annual buoyancy fluxes are a small residual compared to the seasonal fluxes, they will impact the buoyancy budget of the water column along its path. The region within the ACC in the Pacific Ocean tends to lose buoyancy on an annual scale (Fig. 4f), and stratification is smallest in the eastern Pacific sector (Fig. 7a). This decrease in stratification could be partially attributed to the annual loss of buoyancy. In the southeastern Pacific sector, the low stratification of the upper ocean during summer is also linked to enhanced vertical diffusivity in the upper ocean (Sloyan et al., 2010).

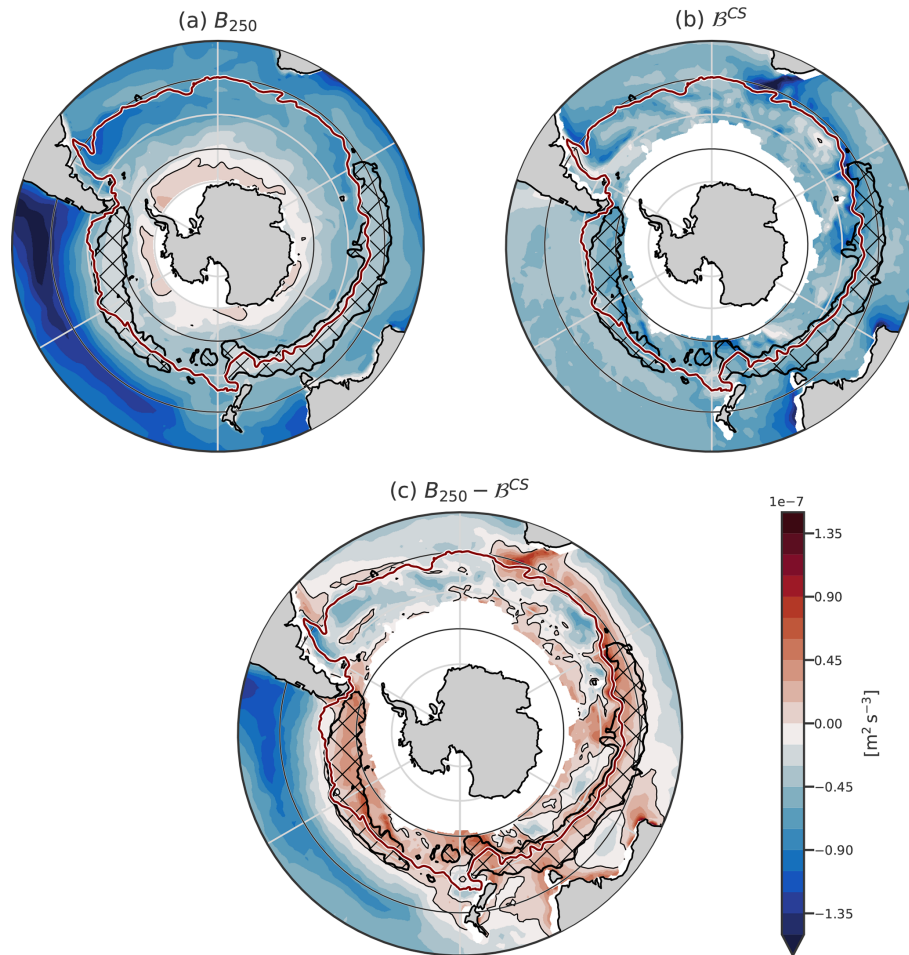


Figure 11. The same as Fig. 7 but using α_0 in computations. Hence, panel (c) represents where the ocean could form the DMB if the TEC was constant. The hatching represents the observed DMB. The region with sea ice around Antarctica is masked in white.

The decrease in the TEC in cold water dampens the effect of the heat component of the buoyancy fluxes. This also decreases the contribution of temperature to stratification. Using a constant TEC for the calculation of buoyancy fluxes, we have shown that the region of large buoyancy loss would be located further poleward, while the stratification induced by temperature would increase if the TEC was constant. As a result of these two opposite effects, the DMB's southern boundary would be located further poleward. This theoretical result has previously been observed in idealised model runs with various values for the polar TEC (Caneill et al., 2022). In line with Roquet et al. (2022), we find that by restraining the deepening of the ML, the variations of the TEC strongly limit the rates of exchange between the surface and the ocean interior. South of the ACC, the impact of temperature is to decrease stratification beneath the winter mixed layer (Pollard et al., 2002). A higher TEC would amplify this effect, resulting in reduced stratification. Furthermore, a higher value of the TEC would enhance the impact of heat loss on buoyancy loss. Thus, climate change and an increase in the (sub)polar

ocean temperature may lead to a further southward extent of the DMB.

A direct implication of our study is that one should not convert buoyancy and freshwater fluxes into heat fluxes using constant TEC. It is important to retain the scaling effect of the TEC on the heat component of the buoyancy fluxes. Taking the annual heat flux and converting it to buoyancy flux using the mean TEC or taking the mean buoyancy flux is not equivalent, as described by Schanze and Schmitt (2013). Thus, when studying stratification, heat and freshwater fluxes need to be converted into buoyancy or density fluxes to accurately quantify their effects on density.

In summary, this study provides a global view of the formation of the deep mixing band in the Southern Ocean. The balance between (i) stratification at the end of summer and (ii) buoyancy loss during the cooling season is sufficient to explain the formation of the DMB, its position, and its width. The reduction in the thermal expansion coefficient value in cold water limits the influence of heat fluxes on buoyancy fluxes. Consequently, despite the large loss of heat in win-

ter, stratification cannot be significantly eroded south of the actual DMB. The small stratification of the southeastern Pacific sector of the ACC is easily eroded, and despite the small winter buoyancy loss in this region, deep MLs are formed in winter.

Appendix A: Correction of heat fluxes

This appendix assesses the validity of the correction on heat fluxes we have applied. Due to the heat imbalance of OAflux, without correction the ocean gains too much heat compared to ECCO (Fig. A1). This is particularly visible in the SO: without correction, almost all the SO gains heat on average, whereas ECCO and our adjusted product show more patchiness and variability. This excess of heat gain is also visible in the buoyancy fluxes (Fig. A1d–f). For example, without the heat correction all Pacific sectors of the SO gain heat, while in ECCO and after correction a small band of buoyancy loss is present. The comparison of the adjusted product with ECCO allows us to have confidence that our computations represent the climatological state of the SO well.

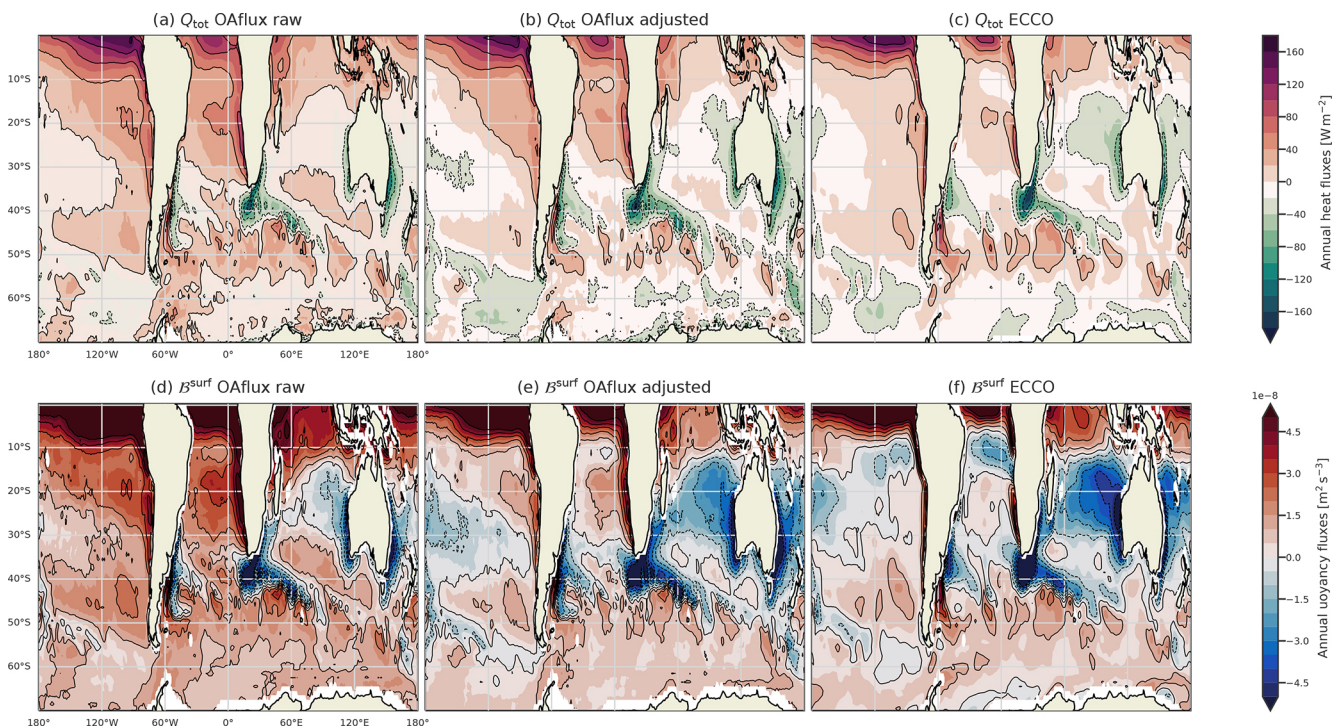


Figure A1. Heat fluxes (a, b, c) and surface buoyancy fluxes (d, e, f) are presented. The first column is the climatology annual mean without any correction, the second column is with our adjustment, and the third column has been computed with the fluxes from ECCO.

Appendix B: Extra maps of buoyancy fluxes

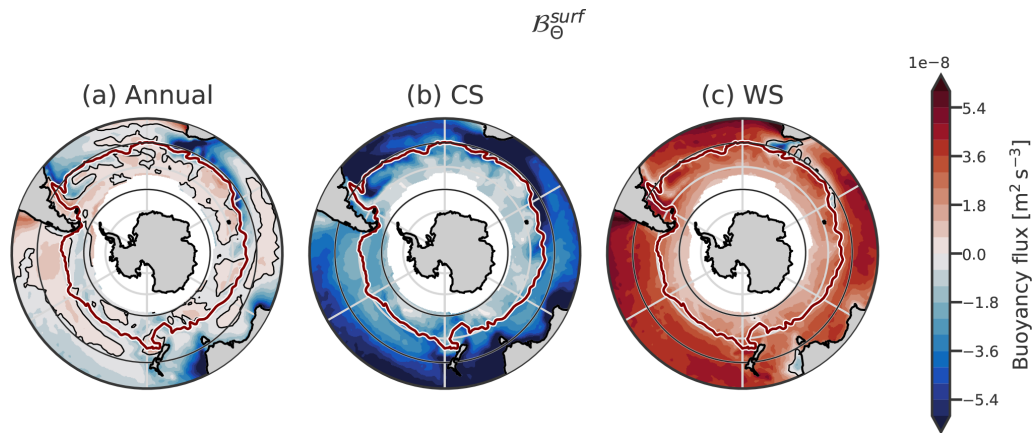


Figure B1. Climatology of the annual, cooling season, and warming season surface heat component of the buoyancy flux.

Appendix C: Comparison with different thresholds for the DMB definition and the columnar buoyancy

The results of this study are not sensitive to the value of the threshold used for defining the DMB (250 m in this study). Reproducing Fig. 7c using different thresholds (200 and 350 m, respectively) does not change the main result: the balance between the buoyancy loss and the stratification predicts the location and shape of the DMB accurately away from the western boundary currents.

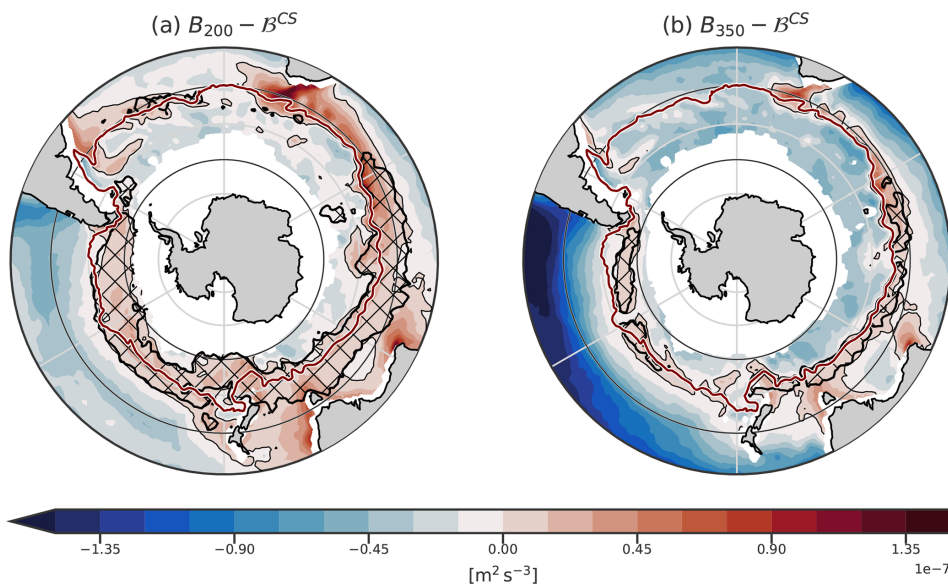


Figure C1. Balance between the columnar buoyancy and buoyancy loss using a depth of (a) 200 and (b) 350 m as threshold for the DMB (hatched area) and columnar buoyancy (B_{200} and B_{350} , respectively).

Code and data availability. ECCO has been downloaded from <https://ecco.jpl.nasa.gov/drive> (last access: 17 October 2023) and <https://doi.org/10.5281/zenodo.4533349> (ECCO Consortium et al., 2022, 2021).

OAflux has been downloaded from ftp://ftp.whoi.edu/pub/science/oaflux/data_v3/monthly/ (last access: 24 February 2022, Yu and Weller, 2007).

ISCCP-FH MPF has been downloaded from https://isccp.giss.nasa.gov/pub/flux-fh/tar-nc4_MPF/ (last access: 1 March 2022, Schiffer and Rossow, 1983; Rossow and Schiffer, 1999).

GPCP has been downloaded from <https://www.ncei.noaa.gov/data/global-precipitation-climatology-project-gpcp-monthly/> (last access: 1 March 2022, Adler et al., 2018).

The “Global Ocean Wind L492 Reprocessed 6 hourly Observations” was replaced in November 2022 by the Global Ocean Hourly Reprocessed Sea Surface Wind and Stress from Scatterometer and Model, EU Copernicus Marine Service Information (CMEMS), Marine Data Store (MDS), <https://doi.org/10.48670/moi-00185> (EU Copernicus Marine Service Information, 2023a). The data have been downloaded from <https://data-cersat.ifremer.fr/data/ocean-wind/mwf/mwf-blended/reprocessing/v6/> (last access: 2 October 2023).

ARMOR3D with <https://doi.org/10.48670/moi-00052> (EU Copernicus Marine Service Information, 2023b) has been downloaded from ftp://nrt.cmems-du.eu/Core/MULTIOBS_GLO_PHY_TSUV_3D_MYNRT_015_012/dataset-armor-3d-rep-weekly.

MIMOC has been downloaded from <http://www.pmel.noaa.gov/mimoc> (last access: 9 December 2021, Schmidtko et al., 2013).

The MLD from de Boyer Montégut (2023) based on the work of de Boyer Montégut (2004) has been downloaded from <https://www.seanoe.org/data/00806/91774/data/103667.tar> (last access: 1 August 2023).

The scripts used to make the figures are shared on GitLab: <https://gitlab.com/rcaneill/caneill-et-al-OS-SO-DMB> (last access: 4 January 2024). The scripts, the data necessary to reproduce the figures, the container with the computing environment, the figures, and the climatologies are archived on Zenodo: <https://doi.org/10.5281/zenodo.10458427> (Caneill, 2024). All the analyses and figures are reproducible within a few steps.

Author contributions. All authors contributed to the study conception. RC conducted analyses. RC prepared the manuscript with contributions from all co-authors.

Competing interests. The contact author has declared that none of the authors has any competing interests.

Disclaimer. Publisher’s note: Copernicus Publications remains neutral with regard to jurisdictional claims made in the text, published maps, institutional affiliations, or any other geographical representation in this paper. While Copernicus Publications makes every effort to include appropriate place names, the final responsibility lies with the authors.

Acknowledgements. The analyses that led to this publication are based on snakemake (Mölder et al., 2021), xarray (Hoyer and Hamman, 2017; Hoyer et al., 2023), xgcm (Abernathey et al., 2022), and cf-xarray (Cherian et al., 2023), and thermodynamic computations were made using gsw-xarray, the xarray wrapper around GSW-Python (McDougall and Barker, 2011; Caneill and Barna, 2023).

This publication is based upon the WHOI OAFlux datasets supported by NOAA’s Global Ocean Monitoring and Observing (GOMO) Program and NASA’s Making Earth System Data Records for Use in Research Environments (MEaSUREs) Program.

We thank the two reviewers, Qian Li and Justin Small, for their comments and questions that helped to improve the paper.

Financial support. The article processing charges for this open-access publication were covered by the Gothenburg University Library.

Review statement. This paper was edited by Ilker Fer and reviewed by Qian Li and Justin Small.

References

- Aagaard, K. and Carmack, E. C.: The role of sea ice and other fresh water in the Arctic circulation, *J. Geophys. Res.*, 94, 14485, <https://doi.org/10.1029/JC094iC10p14485>, 1989.
- Abernathey, R. P., Busecke, J. J. M., Smith, T. A., Deauna, J. D., Banihirwe, A., Nicholas, T., Fernandes, F., James, B., Dussin, R., Cherian, D. A., Caneill, R., Sinha, A., Uieda, L., Rath, W., Balwada, D., Constantinou, N. C., Ponte, A., Zhou, Y., Uchida, T., and Thielen, J.: xgcm, Zenodo [code], <https://doi.org/10.5281/zenodo.7348619>, 2022.
- Adler, R., Sapiano, M., Huffman, G., Wang, J.-J., Gu, G., Bolvin, D., Chiu, L., Schneider, U., Becker, A., Nelkin, E., Xie, P., Ferraro, R., and Shin, D.-B.: The Global Precipitation Climatology Project (GPCP) Monthly Analysis (New Version 2.3) and a Review of 2017 Global Precipitation, *Atmosphere*, 9, 138, <https://doi.org/10.3390/atmos9040138>, 2018.
- Belkin, I. M. and Gordon, A. L.: Southern Ocean fronts from the Greenwich meridian to Tasmania, *J. Geophys. Res.-Oceans*, 101, 3675–3696, <https://doi.org/10.1029/95JC02750>, 1996.
- Bryan, F.: High-latitude salinity effects and interhemispheric thermohaline circulations, *Nature*, 323, 301–304, <https://doi.org/10.1038/323301a0>, 1986.
- Caneill, R.: rcaneill/caneill-et-al-OS-SO-DMB, Zenodo [code], <https://doi.org/10.5281/zenodo.10458818>, 2024.
- Caneill, R. and Barna, A.: gsw-xarray, Zenodo [code], <https://doi.org/10.5281/zenodo.8297619>, 2023.
- Caneill, R., Roquet, F., Madec, G., and Nycander, J.: The Polar Transition from Alpha to Beta Regions Set by a Surface Buoyancy Flux Inversion, *J. Phys. Oceanogr.*, 52, 1887–1902, <https://doi.org/10.1175/JPO-D-21-0295.1>, 2022.
- Carmack, E. C.: The alpha/beta ocean distinction: A perspective on freshwater fluxes, convection, nutrients and productivity in high-latitude seas, *Deep-Sea Res. Pt. II*, 54, 2578–2598, <https://doi.org/10.1016/j.dsr2.2007.08.018>, 2007.

- Cerovečki, I. and Mazloff, M. R.: The Spatiotemporal Structure of Diabatic Processes Governing the Evolution of Subantarctic Mode Water in the Southern Ocean, *J. Phys. Oceanogr.*, 46, 683–710, <https://doi.org/10.1175/JPO-D-14-0243.1>, 2016.
- Cerovečki, I., Talley, L. D., and Mazloff, M. R.: A Comparison of Southern Ocean Air–Sea Buoyancy Flux from an Ocean State Estimate with Five Other Products, *J. Climate*, 24, 6283–6306, <https://doi.org/10.1175/2011JCLI3858.1>, 2011.
- Cerovečki, I., Talley, L. D., Mazloff, M. R., and Maze, G.: Subantarctic Mode Water Formation, Destruction, and Export in the Eddy-Permitting Southern Ocean State Estimate, *J. Phys. Oceanogr.*, 43, 1485–1511, <https://doi.org/10.1175/JPO-D-12-0121.1>, 2013.
- Cerovečki, I., Meijers, A. J. S., Mazloff, M. R., Gille, S. T., Tamsitt, V. M., and Holland, P. R.: The Effects of Enhanced Sea Ice Export from the Ross Sea on Recent Cooling and Freshening of the Southeast Pacific, *J. Climate*, 32, 2013–2035, <https://doi.org/10.1175/JCLI-D-18-0205.1>, 2019.
- Cherian, D., Almansi, M., Bourgault, P., Thyng, K., Thielen, J., Magin, J., Aoun, A., Bunttemeyer, L., Caneill, R., Davis, L., Fernandes, F., Hauser, M., Heerdegen, A., Kent, J., Mankoff, K., Müller, S., Schupfner, M., Vo, T., and Haëck, C.: cf_xarray, Zenodo [code], <https://doi.org/10.5281/zenodo.8152257>, 2023.
- Czaja, A. and Marshall, J.: Why is there net surface heating over the Antarctic Circumpolar Current?, *Ocean Dynam.*, 65, 751–760, <https://doi.org/10.1007/s10236-015-0830-1>, 2015.
- de Boyer Montégut, C.: Mixed layer depth over the global ocean: An examination of profile data and a profile-based climatology, *J. Geophys. Res.*, 109, C12003, <https://doi.org/10.1029/2004JC002378>, 2004.
- de Boyer Montégut, C.: Mixed layer depth climatology computed with a density threshold criterion of 0.03 kg/m^3 from 10 m depth value, SEANOE [data set], <https://doi.org/10.17882/91774>, 2023.
- Dong, S., Gille, S. T., and Sprintall, J.: An Assessment of the Southern Ocean Mixed Layer Heat Budget, *J. Climate*, 20, 4425–4442, <https://doi.org/10.1175/JCLI4259.1>, 2007.
- Dong, S., Sprintall, J., Gille, S. T., and Talley, L.: Southern Ocean mixed-layer depth from Argo float profiles, *J. Geophys. Res.*, 113, C06013, <https://doi.org/10.1029/2006JC004051>, 2008.
- DuVivier, A. K., Large, W. G., and Small, R. J.: Argo Observations of the Deep Mixing Band in the Southern Ocean: A Salinity Modeling Challenge, *J. Geophys. Res.-Oceans*, 123, 7599–7617, <https://doi.org/10.1029/2018JC014275>, 2018.
- ECCO Consortium, Fukumori, I., Wang, O., Fenty, I., Forget, G., Heimbach, P., and Ponte, R. M.: ECCO Central Estimate (Version 4 Release 4), <https://ecco.jpl.nasa.gov/drive>, last access: 15 March 2022.
- ECCO Consortium, Fukumori, I., Wang, O., Fenty, I., Forget, G., Heimbach, P., and Ponte, R.: Synopsis of the ECCO central production global ocean and sea-ice state estimate (version 4 release 4), Zenodo [code], <https://doi.org/10.5281/zenodo.4533349>, 2021.
- EU Copernicus Marine Service Information (CMEMS): Global Ocean Hourly Reprocessed Sea Surface Wind and Stress from Scatterometer and Mode, Marine Data Store (MDS) [data set], <https://doi.org/10.48670/moi-00185> 2023a.
- EU Copernicus Marine Service Information (CMEMS): Multi Observation Global Ocean 3D Temperature Salinity Height Geostrophic Current and MLD, Marine Data Store (MDS) [data set], <https://doi.org/10.48670/moi-00052>, 2023b.
- Faure, V. and Kawai, Y.: Heat and salt budgets of the mixed layer around the Subarctic Front of the North Pacific Ocean, *J. Oceanogr.*, 71, 527–539, <https://doi.org/10.1007/s10872-015-0318-0>, 2015.
- Fernández Castro, B., Mazloff, M., Williams, R. G., and Naveira Garabato, A. C.: Subtropical Contribution to Sub-Antarctic Mode Waters, *Geophys. Res. Lett.*, 49, e2021GL097560, <https://doi.org/10.1029/2021GL097560>, 2022.
- Forget, G., Campin, J.-M., Heimbach, P., Hill, C. N., Ponte, R. M., and Wunsch, C.: ECCO version 4: an integrated framework for non-linear inverse modeling and global ocean state estimation, *Geosci. Model Dev.*, 8, 3071–3104, <https://doi.org/10.5194/gmd-8-3071-2015>, 2015.
- Frölicher, T. L., Sarmiento, J. L., Paynter, D. J., Dunne, J. P., Krasting, J. P., and Winton, M.: Dominance of the Southern Ocean in Anthropogenic Carbon and Heat Uptake in CMIP5 Models, *J. Climate*, 28, 862–886, <https://doi.org/10.1175/JCLI-D-14-00117.1>, 2015.
- Garrett, C., Outerbridge, R., and Thompson, K.: Interannual Variability in Meterranean Heat and Buoyancy Fluxes, *J. Climate*, 6, 900–910, [https://doi.org/10.1175/1520-0442\(1993\)006<0900:IVIMHA>2.0.CO;2](https://doi.org/10.1175/1520-0442(1993)006<0900:IVIMHA>2.0.CO;2), 1993.
- Gill, A. E. and Adrian, E.: Atmosphere-ocean dynamics, vol. 30, Academic press, ISBN 9780122835223, 1982.
- Gruber, N., Clement, D., Carter, B. R., Feely, R. A., Van Heuven, S., Hoppema, M., Ishii, M., Key, R. M., Kozyr, A., Lauvset, S. K., Lo Monaco, C., Mathis, J. T., Murata, A., Olsen, A., Perez, F. F., Sabine, C. L., Tanhua, T., and Wanninkhof, R.: The oceanic sink for anthropogenic CO₂ from 1994 to 2007, *Science*, 363, 1193–1199, <https://doi.org/10.1126/science.aau5153>, 2019.
- Guinehut, S., Dhomps, A.-L., Larnicol, G., and Le Traon, P.-Y.: High resolution 3-D temperature and salinity fields derived from in situ and satellite observations, *Ocean Sci.*, 8, 845–857, <https://doi.org/10.5194/os-8-845-2012>, 2012.
- Hanawa, K. and Talley, L. D.: Chapt. 5.4: Mode waters, in: *Ocean Circulation and Climate*, edited by: Siedler, G., Church, J., and Gould, J., vol. 77 of *International Geophysics*, Academic Press, 373–386, [https://doi.org/10.1016/S0074-6142\(01\)80129-7](https://doi.org/10.1016/S0074-6142(01)80129-7), 2001.
- Herrmann, M., Somot, S., Sevault, F., Estournel, C., and Déqué, M.: Modeling the deep convection in the northwestern Mediterranean Sea using an eddy-permitting and an eddy-resolving model: Case study of winter 1986–1987, *J. Geophys. Res.*, 113, C04011, <https://doi.org/10.1029/2006JC003991>, 2008.
- Hieronymus, M. and Nycander, J.: The Buoyancy Budget with a Nonlinear Equation of State, *J. Phys. Oceanogr.*, 43, 176–186, <https://doi.org/10.1175/JPO-D-12-063.1>, 2013.
- Holland, P. R. and Kwok, R.: Wind-driven trends in Antarctic sea-ice drift, *Nat. Geosci.*, 5, 872–875, <https://doi.org/10.1038/ngeo1627>, 2012.
- Holte, J. W., Talley, L. D., Chereskin, T. K., and Sloyan, B. M.: The role of air-sea fluxes in Subantarctic Mode Water formation: SAMW FORMATION, *J. Geophys. Res.-Oceans*, 117, C03040, <https://doi.org/10.1029/2011JC007798>, 2012.

- Hoyer, S. and Hamman, J.: xarray: N-D labeled arrays and datasets in Python, *J. Open Res. Softw.*, 5, 1, <https://doi.org/10.5334/jors.148>, 2017.
- Hoyer, S., Roos, M., Joseph, H., Magin, J., Cherian, D., Fitzgerald, C., Hauser, M., Fujii, K., Maussion, F., Imperiale, G., Clark, S., Kleeman, A., Nicholas, T., Kluyver, T., Westling, J., Munroe, J., Amici, A., Barghini, A., Banihirwe, A., Bell, R., Hatfield-Dodds, Z., Abernathy, R., Bovy, B., Omotani, J., Mühlbauer, K., Roszko, M. K., and Wolfram, P. J.: xarray, Zenodo [code], <https://doi.org/10.5281/zenodo.8153447>, 2023.
- IOC, SCOR, and IAPSO: The International thermodynamic equation of seawater – 2010: calculation and use of thermodynamic properties, Intergovernmental Oceanographic Commission, Manuals and Guides, 56, 220, http://teos-10.org/pubs/TEOS-10_Manual.pdf (last access: 12 October 2023), 2015.
- Josey, S. A., Grist, J. P., Mecking, J. V., Moat, B. I., and Schulz, E.: A clearer view of Southern Ocean air–sea interaction using surface heat flux asymmetry, *Philos. T. Roy. Soc. A*, 381, 20220067, <https://doi.org/10.1098/rsta.2022.0067>, 2023.
- Klocker, A., Naveira Garabato, A. C., Roquet, F., De Lavergne, C., and Rintoul, S. R.: Generation of the Internal Pycnocline in the Subpolar Southern Ocean by Wintertime Sea Ice Melting, *J. Geophys. Res.-Oceans*, 128, e2022JC019113, <https://doi.org/10.1029/2022JC019113>, 2023.
- Kostianoy, A. G., Ginzburg, A. I., Frankignoulle, M., and Delille, B.: Fronts in the Southern Indian Ocean as inferred from satellite sea surface temperature data, *J. Marine Syst.*, 45, 55–73, <https://doi.org/10.1016/j.jmarsys.2003.09.004>, 2004.
- Lascaratos, A. and Nittis, K.: A high-resolution three-dimensional numerical study of intermediate water formation in the Levantine Sea, *J. Geophys. Res.-Oceans*, 103, 18497–18511, <https://doi.org/10.1029/98JC01196>, 1998.
- Lee, M.-M., Nurser, A. J. G., Stevens, I., and Sallée, J.-B.: Subduction over the Southern Indian Ocean in a High-Resolution Atmosphere–Ocean Coupled Model, *J. Climate*, 24, 3830–3849, <https://doi.org/10.1175/2011JCLI3888.1>, 2011.
- Lenn, Y.-D. and Chereskin, T. K.: Observations of Ekman Currents in the Southern Ocean, *J. Phys. Oceanogr.*, 39, 768–779, <https://doi.org/10.1175/2008JPO3943.1>, 2009.
- Li, Q. and England, M. H.: Tropical Indo-Pacific Teleconnections to Southern Ocean Mixed Layer Variability, *Geophys. Res. Lett.*, 47, e2020GL088466, <https://doi.org/10.1029/2020GL088466>, 2020.
- Li, Q. and Lee, S.: A Mechanism of Mixed Layer Formation in the Indo–Western Pacific Southern Ocean: Preconditioning by an Eddy-Driven Jet-Scale Overturning Circulation, *J. Phys. Oceanogr.*, 47, 2755–2772, <https://doi.org/10.1175/JPO-D-17-0006.1>, 2017.
- Li, Z., Groeskamp, S., Cerovečki, I., and England, M. H.: The Origin and Fate of Antarctic Intermediate Water in the Southern Ocean, *J. Phys. Oceanogr.*, 52, 2873–2890, <https://doi.org/10.1175/JPO-D-21-0221.1>, 2022.
- Li, Z., England, M. H., and Groeskamp, S.: Recent acceleration in global ocean heat accumulation by mode and intermediate waters, *Nat. Commun.*, 14, 6888, <https://doi.org/10.1038/s41467-023-42468-z>, 2023.
- McDougall, T. J. and Barker, P. M.: Getting started with TEOS-10 and the Gibbs Seawater (GSW) Oceanographic Toolbox, SCOR/IAPSO WG127, ISBN 978-0-646-55621-5, 2011.
- Mölder, F., Jablonski, K., Letcher, B., Hall, M., Tomkins-Tinch, C., Sochat, V., Forster, J., Lee, S., Twardziok, S., Kanitz, A., Wilm, A., Holtgrewe, M., Rahmann, S., Nahsen, S., and Köster, J.: Sustainable data analysis with Snakemake, *F1000Research*, 10, 33, <https://doi.org/10.12688/f1000research.29032.1>, 2021.
- Naveira Garabato, A. C., Jullion, L., Stevens, D. P., Heywood, K. J., and King, B. A.: Variability of Subantarctic Mode Water and Antarctic Intermediate Water in the Drake Passage during the Late-Twentieth and Early-Twenty-First Centuries, *J. Climate*, 22, 3661–3688, <https://doi.org/10.1175/2009JCLI2621.1>, 2009.
- Nycander, J., Hieronymus, M., and Roquet, F.: The nonlinear equation of state of sea water and the global water mass distribution: Global Water Mass Distribution, *Geophys. Res. Lett.*, 42, 7714–7721, <https://doi.org/10.1002/2015GL065525>, 2015.
- Orsi, A. H., Whitworth, T., and Nowlin, W. D.: On the meridional extent and fronts of the Antarctic Circumpolar Current, *Deep-Sea Res. Pt. I*, 42, 641–673, [https://doi.org/10.1016/0967-0637\(95\)00021-W](https://doi.org/10.1016/0967-0637(95)00021-W), 1995.
- Park, Y., Park, T., Kim, T., Lee, S., Hong, C., Lee, J., Rio, M., Pujol, M., Ballarotta, M., Durand, I., and Provost, C.: Observations of the Antarctic Circumpolar Current Over the Udintsev Fracture Zone, the Narrowest Choke Point in the Southern Ocean, *J. Geophys. Res.-Oceans*, 124, 4511–4528, <https://doi.org/10.1029/2019JC015024>, 2019.
- Pauthenet, E., Roquet, F., Madec, G., and Nerini, D.: A Linear Decomposition of the Southern Ocean Thermohaline Structure, *J. Phys. Oceanogr.*, 47, 29–47, <https://doi.org/10.1175/JPO-D-16-0083.1>, 2017.
- Pellichero, V., Sallée, J.-B., Chapman, C. C., and Downes, S. M.: The southern ocean meridional overturning in the sea-ice sector is driven by freshwater fluxes, *Nat. Commun.*, 9, 1789, <https://doi.org/10.1038/s41467-018-04101-2>, 2018.
- Pollard, R., Lucas, M., and Read, J.: Physical controls on biogeochemical zonation in the Southern Ocean, *Deep-Sea Res. Pt. II*, 49, 3289–3305, [https://doi.org/10.1016/S0967-0645\(02\)00084-X](https://doi.org/10.1016/S0967-0645(02)00084-X), 2002.
- Qiu, B. and Kelly, K. A.: Upper-Ocean Heat Balance in the Kuroshio Extension Region, *J. Phys. Oceanogr.*, 23, 2027–2041, [https://doi.org/10.1175/1520-0485\(1993\)023<2027:UOHBIT>2.0.CO;2](https://doi.org/10.1175/1520-0485(1993)023<2027:UOHBIT>2.0.CO;2), 1993.
- Rintoul, S. R.: The global influence of localized dynamics in the Southern Ocean, *Nature*, 558, 209–218, <https://doi.org/10.1038/s41586-018-0182-3>, 2018.
- Rintoul, S. R. and England, M. H.: Ekman Transport Dominates Local Air–Sea Fluxes in Driving Variability of Subantarctic Mode Water, *J. Phys. Oceanogr.*, 32, 1308–1321, [https://doi.org/10.1175/1520-0485\(2002\)032<1308:ETDLAS>2.0.CO;2](https://doi.org/10.1175/1520-0485(2002)032<1308:ETDLAS>2.0.CO;2), 2002.
- Roach, C. J., Phillips, H. E., Bindoff, N. L., and Rintoul, S. R.: Detecting and Characterizing Ekman Currents in the Southern Ocean, *J. Phys. Oceanogr.*, 45, 1205–1223, <https://doi.org/10.1175/JPO-D-14-0115.1>, 2015.
- Roemmich, D., Church, J., Gilson, J., Monselesan, D., Sutton, P., and Wijffels, S.: Unabated planetary warming and its ocean structure since 2006, *Nat. Clim. Change*, 5, 240–245, <https://doi.org/10.1038/nclimate2513>, 2015.
- Roquet, F., Madec, G., Brodeau, L., and Nycander, J.: Defining a Simplified Yet “Realistic” Equation of State for Seawater, *J.*

- Phys. Oceanogr., 45, 2564–2579, <https://doi.org/10.1175/JPO-D-15-0080.1>, 2015.
- Roquet, F., Ferreira, D., Caneill, R., Schlesinger, D., and Madec, G.: Unique thermal expansion properties of water key to the formation of sea ice on Earth, *Sci. Adv.*, 8, eabq0793, <https://doi.org/10.1126/sciadv.abq0793>, 2022.
- Rossow, W. B. and Schiffer, R. A.: Advances in Understanding Clouds from ISCCP, *B. Am. Meteorol. Soc.*, 80, 2261–2287, [https://doi.org/10.1175/1520-0477\(1999\)080<2261:AIUCFI>2.0.CO;2](https://doi.org/10.1175/1520-0477(1999)080<2261:AIUCFI>2.0.CO;2), 1999.
- Sabine, C. L., Feely, R. A., Gruber, N., Key, R. M., Lee, K., Bullister, J. L., Wanninkhof, R., Wong, C. S., Wallace, D. W. R., Tilbrook, B., Millero, F. J., Peng, T.-H., Kozyr, A., Ono, T., and Rios, A. F.: The Oceanic Sink for Anthropogenic CO₂, *Science*, 305, 367–371, <https://doi.org/10.1126/science.1097403>, 2004.
- Sallée, J.-B., Wienders, N., Speer, K., and Morrow, R.: Formation of subantarctic mode water in the southeastern Indian Ocean, *Ocean Dynam.*, 56, 525–542, <https://doi.org/10.1007/s10236-005-0054-x>, 2006.
- Sallée, J.-B., Morrow, R., and Speer, K.: Eddy heat diffusion and Subantarctic Mode Water formation, *Geophys. Res. Lett.*, 35, L05607, <https://doi.org/10.1029/2007GL032827>, 2008.
- Sallée, J.-B., Speer, K., Rintoul, S., and Wijffels, S.: Southern Ocean Thermocline Ventilation, *J. Phys. Oceanogr.*, 40, 509–529, <https://doi.org/10.1175/2009JPO4291.1>, 2010.
- Schanze, J. J. and Schmitt, R. W.: Estimates of Cabbelling in the Global Ocean, *J. Phys. Oceanogr.*, 43, 698–705, <https://doi.org/10.1175/JPO-D-12-0119.1>, 2013.
- Schiffer, R. A. and Rossow, W. B.: The International Satellite Cloud Climatology Project (ISCCP): The first project of the World Climate Research Programme, *B. Am. Meteorol. Soc.*, 64, 779–784, 1983.
- Schmidtko, S., Johnson, G. C., and Lyman, J. M.: MIMOC: A global monthly isopycnal upper-ocean climatology with mixed layers: MIMOC, *J. Geophys. Res.-Oceans*, 118, 1658–1672, <https://doi.org/10.1002/jgrc.20122>, 2013.
- Sloyan, B. M. and Rintoul, S. R.: Circulation, Renewal, and Modification of Antarctic Mode and Intermediate Water, *J. Phys. Oceanogr.*, 31, 1005–1030, [https://doi.org/10.1175/1520-0485\(2001\)031<1005:CRAMOA>2.0.CO;2](https://doi.org/10.1175/1520-0485(2001)031<1005:CRAMOA>2.0.CO;2), 2001.
- Sloyan, B. M., Talley, L. D., Chereskin, T. K., Fine, R., and Holte, J.: Antarctic Intermediate Water and Subantarctic Mode Water Formation in the Southeast Pacific: The Role of Turbulent Mixing, *J. Phys. Oceanogr.*, 40, 1558–1574, <https://doi.org/10.1175/2010JPO4114.1>, 2010.
- Small, R. J., DuVivier, A. K., Whitt, D. B., Long, M. C., Grooms, I., and Large, W. G.: On the control of subantarctic stratification by the ocean circulation, *Clim. Dynam.*, 56, 299–327, <https://doi.org/10.1007/s00382-020-05473-2>, 2021.
- Song, X.: Explaining the Zonal Asymmetry in the Air-Sea Net Heat Flux Climatology Over the Antarctic Circumpolar Current, *J. Geophys. Res.-Oceans*, 125, e2020JC016215, <https://doi.org/10.1029/2020JC016215>, 2020.
- Speer, K., Rintoul, S. R., and Sloyan, B.: The Diabatic Deacon Cell, *J. Phys. Oceanogr.*, 30, 3212–3222, [https://doi.org/10.1175/1520-0485\(2000\)030<3212:TDDC>2.0.CO;2](https://doi.org/10.1175/1520-0485(2000)030<3212:TDDC>2.0.CO;2), 2000.
- Sterl, M. F. and De Jong, M. F.: Restratification Structure and Processes in the Irminger Sea, *J. Geophys. Res.-Oceans*, 127, e2022JC019126, <https://doi.org/10.1029/2022JC019126>, 2022.
- Swart, S., Gille, S. T., Delille, B., Josey, S., Mazloff, M., Newman, L., Thompson, A. F., Thomson, J., Ward, B., Du Plessis, M. D., Kent, E. C., Girtton, J., Gregor, L., Heil, P., Hyder, P., Pezzi, L. P., De Souza, R. B., Tamsitt, V., Weller, R. A., and Zappa, C. J.: Constraining Southern Ocean Air-Sea-Ice Fluxes Through Enhanced Observations, *Front. Mar. Sci.*, 6, 421, <https://doi.org/10.3389/fmars.2019.00421>, 2019.
- Tamsitt, V., Talley, L. D., Mazloff, M. R., and Cerovečki, I.: Zonal Variations in the Southern Ocean Heat Budget, *J. Climate*, 29, 6563–6579, <https://doi.org/10.1175/JCLI-D-15-0630.1>, 2016.
- Virtanen, P., Gommers, R., Oliphant, T. E., Haberland, M., Reddy, T., Cournapeau, D., Burovski, E., Peterson, P., Weckesser, W., Bright, J., van der Walt, S. J., Brett, M., Wilson, J., Millman, K. J., Mayorov, N., Nelson, A. R. J., Jones, E., Kern, R., Larson, E., Carey, C. J., Polat, İ., Feng, Y., Moore, E. W., VanderPlas, J., Laxalde, D., Perktold, J., Cimrman, R., Henriksen, I., Quintero, E. A., Harris, C. R., Archibald, A. M., Ribeiro, A. H., Pedregosa, F., van Mulbregt, P., and SciPy 1.0 Contributors: SciPy 1.0: Fundamental Algorithms for Scientific Computing in Python, *Nat. Meth.*, 17, 261–272, <https://doi.org/10.1038/s41592-019-0686-2>, 2020.
- Wang, J., Mazloff, M. R., and Gille, S. T.: Pathways of the Agulhas waters poleward of 29°S, *J. Geophys. Res.-Oceans*, 119, 4234–4250, <https://doi.org/10.1002/2014JC010049>, 2014.
- Yang, J.: The Seasonal Variability of the Arctic Ocean Ekman Transport and Its Role in the Mixed Layer Heat and Salt Fluxes, *J. Climate*, 19, 5366–5387, <https://doi.org/10.1175/JCLI3892.1>, 2006.
- Yeager, S. G. and Large, W. G.: Observational Evidence of Winter Spice Injection, *J. Phys. Oceanogr.*, 37, 2895–2919, <https://doi.org/10.1175/2007JPO3629.1>, 2007.
- Yu, L. and Weller, R. A.: Objectively Analyzed Air–Sea Heat Fluxes for the Global Ice-Free Oceans (1981–2005), *B. Am. Meteorol. Soc.*, 88, 527–540, <https://doi.org/10.1175/BAMS-88-4-527>, 2007.
- Zahariev, K. and Garrett, C.: An Apparent Surface Buoyancy Flux Associated with the Nonlinearity of the Equation of State, *J. Phys. Oceanogr.*, 27, 362–368, [https://doi.org/10.1175/1520-0485\(1997\)027<0362:AASBFA>2.0.CO;2](https://doi.org/10.1175/1520-0485(1997)027<0362:AASBFA>2.0.CO;2), 1997.